Analysis of a Beat-Frequency Sensor Operating Near the Locking Boundary

Mabel Pontón, *Member, IEEE*, Sergio Sancho, *Senior Member, IEEE*, and Almudena Suárez, *Fellow, IEEE*

***Abstract*—We present an in-depth investigation of a beat-frequency sensor based on an injected oscillator operating near its locking boundaries. Under these conditions, the beat frequency exhibits higher sensitivity to the material under test (MUT) than the free-running oscillation frequency. We will derive a general expression for the beat frequency as influenced by the MUT. This expression depends on an admittance function that can be extracted from harmonic-balance (HB) simulations, so it can be applied to oscillators of arbitrary complexity. In the new formulation, both the free-running solution and the locking bandwidth will vary with the sensing parameter. We will analyze in depth the beat-frequency curve relative to the parameter under test, as well as its dependence on the design elements. We will also present a new method to establish the selected locking boundary at a suitable value for the anticipated MUT variation range. Additionally, we will demonstrate the potential to sense at a multiple of the beat frequency, thereby increasing frequency sensitivity. For the first time to our knowledge, we will analyze the oscillator phase noise when operating near the locking boundaries by means of a perturbation formulation in the frequency domain. The methods will be illustrated through their application to a cubic-nonlinearity oscillator, enabling a deep theoretical insight, and to a realistic transistor-based oscillator with the MUT placed on top of a capacitive transmission line.**

***Index Terms*—Envelope transient, injection locking, noise analysis.**

I. Introduction

MICROWAVE sensors have the advantages of high sensitivity to the material properties, low cost, and versatility [1], [2], [3], [4], [5], [6], [7], [8] since they can be applied to a broad range of materials, including solids, liquids, and powders. Sensors based on oscillators enable a compact implementation thanks to their direct readout capabilities [9], [10], [11], [12], [13], [14]. Due to their inherent gain, they may also provide a higher sensitivity in comparison with their passive counterparts. Most oscillator-based sensors operate in a free-running regime and rely on the variation of the oscillation frequency with the material under test (MUT). However, a few recent works have proposed sensors based on injection-locked oscillators [15], [16], [17], [18], [19], [20], [21], [22]. In [15], [16], [17], and [18], the sensing relies on the detection of the phase shift between two oscillator circuits locked by the same input source when only one of the oscillators is affected by the sensing parameter. When using one oscillator only, the sensing may be based on the variation of the central frequency of the locking band [19] or on the variation of both the central frequency and bandwidth [20], [21]. We should note that under a low input power, the central frequency of the locking band agrees with the free-running one. Thus, the sensitivity will be conditioned by the variation of the oscillator free-running frequency with the MUT. A third sensing mechanism, recently proposed in [22], uses two coupled oscillators in unlocked conditions, but operating near the locking boundary. Unlike [15], [16], [17], [18], [19], [20], and [21], where the oscillator-based sensor operates in a periodic regime, the sensor in [22] operates in a quasi-periodic regime, with two incommensurate fundamental frequencies. The sensed quantity is the frequency difference between the two unlocked oscillations or beat frequency, ω_b, when the MUT affects one oscillator only. As shown in [22], near the locking boundaries, the beat frequency ω_b varies significantly faster than the individual oscillation frequencies, thus enabling a sensitivity gain. The enhanced sensitivity is maintained within a limited range near the locking boundary. Therefore, the concept will be of interest for detecting small MUT variations. The analysis in [22], based on Kuramoto and Araki's model [23], neglects the variation in the oscillation amplitude due to coupling effects. Thus, the model is overly simplified and will have limited accuracy when applied to transistor-based oscillators.

In this work, we will consider an oscillator injected by an independent source, delivering a low input power. As in [22], the oscillator will operate outside the locking range, but near the locking boundaries. The use of an independent source should enable better system controllability and less drift in comparison with two coupled oscillators. With respect to [22], we will present three main novelties: a realistic semianalytical prediction of the beat frequency, a method to set the locking boundary at a suitable value for the anticipated MUT variation range, and an investigation of the oscillator phase noise when operating near the locking boundaries. All these elements are integral to providing a comprehensive understanding of the sensor's operation and capabilities.

We will begin by applying bifurcation theory [24], [25] to understand how the oscillator frequency transforms when

Received 12 November 2024; revised 21 January 2025; accepted 7 March 2025. Date of publication 2 April 2025; date of current version 16 September 2025. This work was supported in part by the Spanish Ministry of Science and Innovation, Ministerio de Ciencia e Innovación (MCIN)/Agencia Estatal de Investigación (AEI)/10.13039/501100011033, under Grant PID2020-116569RB-C31; in part by the Spanish Ministry of Science, Innovation, and Universities, Ministerio de Ciencia, Innovación y Universidades (MICIU)/AEI/10.13039/501100011033, under Grant PID2023-147653OB-C31; and in part by the European Regional Development Fund [ERDF/Fondo Europeo de Desarrollo Regional (FEDER)]. *(Corresponding author: Mabel Pontón.)*

The authors are with the Departamento de Ingeniería de Comunicaciones, Universidad de Cantabria, 39005 Santander, Spain (e-mail: mabel.ponton@unican.es; sanchosm@unican.es; suareza@unican.es).

Digital Object Identifier 10.1109/TMTT.2025.3552963

it surpasses the locking boundaries. Following this, we will derive a realistic, semianalytical expression for the beat frequency as influenced by the MUT. Given the low input amplitude, this expression will be based on a system linearization around the free-running oscillation, as in [26], [27], and [28]. However, unlike [26], [27], and [28], our formulation will depend on a general admittance function, extracted from harmonic-balance (HB) simulations [14], [29]. Thus, the method can be applied to oscillators of arbitrary topology. In the new formulation, both the free-running point and the locking band will vary with the sensing parameter. The results will be compared with circuit-level envelope-transient simulations [30], [31], using a new procedure to determine the beat frequency. We will analyze the spectrum and demonstrate the potential to sense at a multiple of the beat frequency, thereby increasing frequency sensitivity.

We should be able to establish the selected locking boundary at a suitable value for the anticipated MUT variation range. Otherwise, the boundary will vary with the circuit elements and parameters, leaving the designer with no control. To enable this control, we will present a new methodology compatible with commercial HB tools that relies on a bifurcation condition, derived in terms of the sensing parameter. This approach enables us to optimize the beat-frequency sensitivity without modifying the sensing-parameter range.

Finally, we will address phase noise, an undesirable characteristic of oscillator circuits that can degrade both performance and reliability. In quasi-periodic solutions with an autonomously generated fundamental frequency, there is invariance to phase shifts associated with this frequency [32], [33], which will lead to an accumulation of noise perturbations. To the best of our knowledge, we will analyze for the first time the phase-noise spectrum of the unlocked oscillator operating near the locking boundaries, which was identified as a pending research topic in [22]. We will represent the phase perturbation in a Fourier series and derive an equation relating its power spectral density (PSD) with that of the oscillator noise sources in terms of Toeplitz matrices [34]. This will allow an insightful understanding of the evolution of the phase-noise spectrum when varying the beat frequency.

The methods will be illustrated through their application to a cubic-nonlinearity oscillator, which will enable a deep theoretical insight, and to a realistic transistor-based sensor oscillator, which has been manufactured and experimentally characterized. Note that the objective of this work is not to obtain a record sensitivity (which would depend on the original oscillator design), but rather to demonstrate new methods for accurately predicting and enhancing the sensing capabilities when operating near the locking boundaries.

Section II describes the semianalytical formulation for predicting the beat frequency and establishing the upper or lower locking boundary. Section III presents a detailed analytical study of a cubic-nonlinearity oscillator, which functions as a beat-frequency sensor. Section IV describes an analysis and design method, based on harmonic balance, illustrated with a transistor-based oscillator. Finally, Section V presents the phase-noise analysis and characterization.

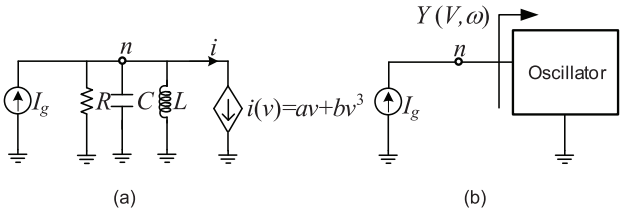

Fig. 1. Injected oscillator. (a) Cubic-nonlinearity oscillator used to get insight into some of the analysis procedures. Element values: $a = -0.03\Omega^{-1}, b = 0.01$ A/V^3, $C = 2.5$ pF, $L = 4$ nH, and $R = 50\ \Omega$. (b) General oscillator considered for the analytical derivations.

II. Semianalytical Formulation of the Beat-Frequency Sensor

Rigorous analysis and design require an understanding of the bifurcation phenomena that define the stable locked-operation intervals of the injected oscillator. These phenomena are general and independent of the specific oscillator. Here, we describe them based on previous works [35], [36], [37] and illustrate them using the circuit shown in Fig. 1(a). Next, we will derive the semianalytical formulations for the beat frequency, the upper and lower locking boundary, and the unlocked spectrum.

A. Bifurcation Phenomena at the Locking Boundaries

The circuit in Fig. 1(a), with a voltage-controlled current source $i(v) = av + bv^3$, where $a < 0$ and $b > 0$, is driven at a constant frequency $f = 1.592$ GHz and the analysis parameter is the capacitor C. The periodic-solution curves, obtained with the method in [20] for different values of the input amplitude I_g, are shown in Fig. 2(a). For the lower I_g values, we have two disjoint periodic curves, as in the case of $I_g = 3$ mA. The closed curve is composed of the locked solutions and is delimited by two turning points, at which the curve exhibits an infinite slope, denoted as T_1 and T_2. At each turning point, a real pole crosses the origin of the complex plane. Thus, either the upper or lower section of the closed curve is stable, whereas the other section is unstable [35], [36], [37]. Here, the upper section is stable. In the low-amplitude curve, the self-oscillation is not excited, and the circuit responds to the input source in a nonautonomous manner. The entire low-amplitude curve is unstable [35], [36], [37]. As I_g increases, the two disconnected curves approach each other and merge at a particular I_g. After merging, the single solution curve exhibits four turning points (denoted as T_1, T_1', T_2, and T_2'), as seen for $I_g = 4.5$ mA. When further increasing I_g, the turning points on each side approach each other and eventually vanish (see the case of $I_g = 7$ mA). Depending on the input amplitude I_g, the stable locked-operation interval is determined by different phenomena: local-global turning-point bifurcations, for low I_g, and secondary Hopf bifurcations, for higher I_g [34], [35].

The local-global turning-point bifurcations occur at lower input amplitudes, typically at the boundaries of closed periodic-solution curves. They are due to the collision of a stable periodic solution [of node type (N)] and an unstable periodic solution [of saddle type (S)] in a turning point at which the stable and unstable manifolds of the two periodic solutions intersect [24], [25]. The intersection gives rise to

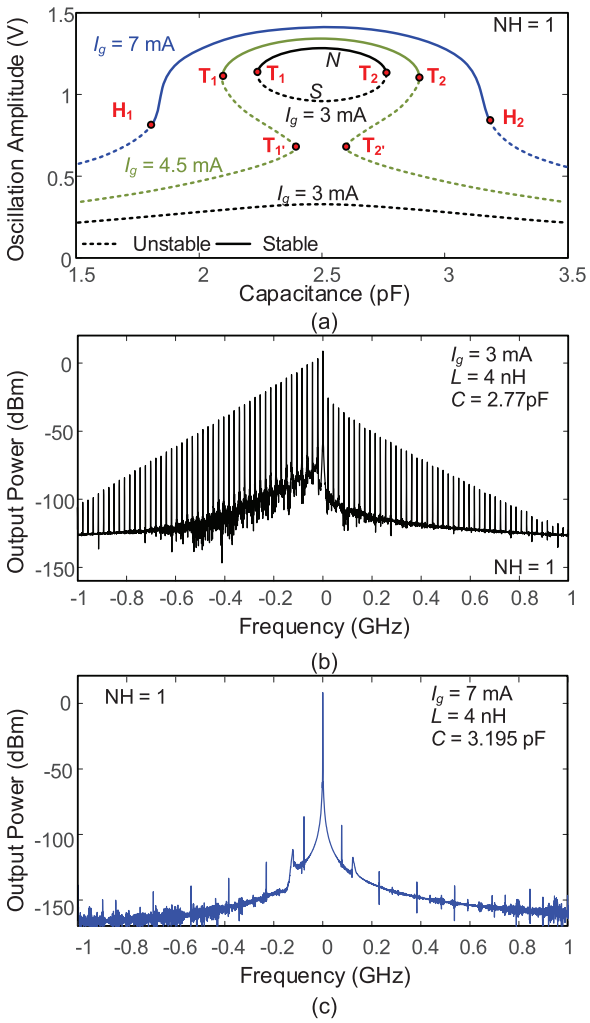

Fig. 2. Bifurcations delimiting the locked-operation intervals, illustrated using the circuit in Fig. 1(a). (a) Periodic-solution curves for three different input amplitudes (I_g) and f = 1.592 GHz versus C. Unstable sections are traced in dashed line. (b) Spectrum just after a local-global turning-point bifurcation, when I_g = 3 mA and C = 2.77 pF. It is centered at the input frequency f. (c) Spectrum just after a Hopf bifurcation when I_g = 7 mA and C = 3.195 pF.

a quasi-periodic solution with two fundamental frequencies, ω and ω_a. The difference ω_b between these two frequencies, known as beat frequency, is $\omega_b = \omega - \omega_a = 0$ at the turning point. Just after the turning point, the spectrum, composed of spectral lines spaced by ω_b, is very dense, as shown in Fig. 2(b), corresponding to C = 2.77 pF and I_g = 3 mA. Note that the represented spectrum is centered at the input frequency ω. The beat frequency grows fast when moving away from the turning point and tends to $\omega_{bo} = \omega - \omega_o$ when the input source has a negligible effect on the oscillation frequency. Unlocking due to local-global turning-point bifurcations can also be obtained after the curve merging [36], [37]. This is the case of T_1 and T_2 at I_g = 4.5 mA in Fig. 2(a). However, as I_g continues to increase, the turning points become simple jump points [36], [37].

The secondary Hopf bifurcations are typically obtained at higher input amplitudes [35], [36], [37]. See H_1 and H_2 at I_g = 7 mA in Fig. 2(a). A pair of complex-conjugate poles ($\sigma \pm j\omega_a$) of the periodic solution at ω crosses the imaginary axis to the right-hand side of the complex plane. This leads to the onset of a quasi-periodic solution with two fundamental frequencies, ω and ω_a, which fulfill $\omega_b = \omega - \omega_a \neq 0$ at the bifurcation point. See the spectrum in Fig. 2(c), for C = 3.195 pF and I_g = 7 mA. The amplitude of the newly generated fundamental frequency ω_a is zero at the secondary Hopf bifurcation and grows in a continuous manner when moving away from it. At the bifurcation, the frequency ω_a tends to be close to the free-running one ω_o, due to the limited impact of the input source for a large difference between ω and ω_o. Thus, we cannot expect a sensitivity gain with respect to free-running operation, unlike the case of unlocking at a local-global turning-point bifurcation.

B. Variation of the Beat Frequency

Our goal, as inferred from Section II-A, is to achieve unlocking through a local-global turning-point bifurcation, which requires the amplitude I_g to be relatively low. We will analyze the dependence of the beat frequency ω_b on the sensing parameter η, which will affect both the free-running oscillation and locking band. We would like to emphasize that although our oscillator is driven by an independent RF source, it operates in an unlocked mode, as the sensing is based on the variation of the beat frequency, that is, the difference between the injection frequency and the self-oscillation frequency (under injection). The oscillator is described with the admittance function $Y(V, \omega)$, calculated at the fundamental frequency at the analysis node n, in terms of the excitation frequency ω and voltage amplitude V [see Fig. 1(b)]. The function $Y(V, \omega)$ can be numerical in nature and extracted from HB simulations. Unlike previous works [26], [27], [28], which assume a dependence $Y(V, \omega) = Y_r(V) + jY_i(\omega)$, our admittance function will have the general form $Y(V, \omega) = Y_r(V, \omega) + jY_i(V, \omega)$, as is typically the case when considering multiple harmonic terms. The general applicability to arbitrary oscillator designs will be demonstrated in Section IV, where we address a single-ended transistor-based oscillator with series feedback.

As stated, the amplitude of the input source I_g will be small. Thus, the oscillation will only undergo small variations in amplitude and frequency with respect to the free-running solution: $V_o(\eta), \omega_o(\eta)$. We will consider small increments in the amplitude, $V_o + \Delta V$, and frequency, $\omega - js$, noting that multiplication by the complex frequency s acts as a time differentiator [37], [38]. The increments are small, so we can expand $Y(V, \omega)$ in a first-order Taylor series about $V_o(\eta), \omega_o(\eta)$. Splitting the resulting complex equation into real and imaginary parts, we obtain

$$\begin{aligned}
&\frac{\partial Y^r\left[V_o(\eta), \omega_o(\eta)\right]}{\partial V}\left[V(t) - V_o(\eta)\right] \\
&\quad + \frac{\partial Y^r\left[V_o(\eta), \omega_o(\eta)\right]}{\partial \omega}\left[\omega + \frac{d\phi}{dt} - \omega_o(\eta)\right] = \frac{I_g}{V_o}\cos\phi(t) \\
&\frac{\partial Y^i\left[V_o(\eta), \omega_o(\eta)\right]}{\partial V}\left[V(t) - V_o(\eta)\right] \\
&\quad + \frac{\partial Y^i\left[V_o(\eta), \omega_o(\eta)\right]}{\partial \omega}\left[\omega + \frac{d\phi}{dt} - \omega_o(\eta)\right] = -\frac{I_g}{V_o}\sin\phi(t)
\end{aligned} \tag{1}$$

where $\phi(t)$ is the phase shift between the analysis node and the input source, the derivative of the amplitude increment $d\Delta V(t)/dt \cong 0$ has been neglected, and the superscripts indicate real and imaginary parts. Solving for $\omega+d\phi/dt-\omega_o(\eta)$, we can write

$$\frac{d\phi(t)}{dt} = -\frac{I_g}{V_o(\eta)} \frac{\sin\left[\phi(t)+\alpha_v(\eta)\right]}{\left|\frac{\partial Y_o(\eta)}{\partial \omega}\right| \sin \alpha_{v\omega}(\eta)} - \Delta\omega(\eta) \tag{2}$$

where $\partial Y_o/\partial V$ and $\partial Y_o/\partial \omega$ are the amplitude and frequency derivatives calculated at the free-running solution, respectively; $\alpha_v = \text{ang}(\partial Y_o/\partial V)$; $\alpha_{v\omega} = \text{ang}(\partial Y_o/\partial \omega) - \text{ang}(\partial Y_o/\partial V)$; and $\Delta\omega(\eta) = \omega - \omega_o(\eta)$. Note that in previous works [22], [23], [24], the angles are assumed to be: $\text{ang}(\partial Y(V_o, \omega_o)/\partial V) = 0$ and $\text{ang}(\partial Y(V_o, \omega_o)/\partial V) = \pi/2$.

Next, we will address the analysis of the locked mode, which is needed to determine or impose the upper or lower locking boundary from which the sensor operates. Under locked conditions, $d\phi/dt = 0$ and (2) simplifies to

$$\omega - \omega_o(\eta) = -B(\eta) \sin\left[\phi + \alpha_v(\eta)\right] \tag{3}$$

where, for notation simplicity, we have introduced the following function $B(\eta)$:

$$B(\eta) = \frac{I_g}{V_o(\eta)} \frac{1}{\left|\frac{\partial Y_o(\eta)}{\partial \omega}\right| \sin \alpha_{v\omega}(\eta)}. \tag{4}$$

Note that the above expression particularizes to the one in [15], [26], [27], and [28] when $\alpha_v = 0$ and $\alpha_{v\omega} = \pi/2$. For each constant φ, the amplitude V (which is also constant) is directly obtained from (1) by solving for the amplitude increment $[V - V_o(\eta)]$ as a function of the terms on the right-hand side: $(I_g/V_o)\cos\phi(t)$ and $-(I_g/V_o)\sin\phi(t)$. This provides

$$V - V_o(\eta) = \frac{I_g}{V_o(\eta)} \frac{1}{\left|\frac{\partial Y_o(\eta)}{\partial V}\right| \sin \alpha_{v\omega}(\eta)} \sin\left[\alpha_\omega(\eta) + \phi\right] \tag{5}$$

where $\alpha_\omega = \text{ang}(\partial Y_o/\partial \omega)$. Due to the sinus function, expression (5) provides two solutions for each ω, with the phases $\phi_1 = \theta - \alpha_v$ and $\phi_2 = \pi - \theta - \alpha_v$, except at the locking boundaries (corresponding to the turning points), where there is only one solution, fulfilling $\phi_1 = \phi_2 = \pm\pi/2 - \alpha_v$. Note that each boundary is obtained for a different sign. The two solutions coexisting for each ω and the two turning points are consistent with the closed solution curve of Fig. 2(a), obtained for small I_g. In the approximation (5), the two solutions have amplitude increments ΔV of the same magnitude and different sign, which is also consistent. If the oscillator is stable in free-running conditions, one solution will be stable and the other will be unstable, as is easily derived by introducing a small perturbation $\delta\phi(t)$ in (2)

$$\delta\dot{\varphi}(t) = -B(\eta)\cos\left[\phi + \alpha_v(\eta)\right]\delta\varphi(t). \tag{6}$$

The stable solutions will fulfill: $\cos[\phi + \alpha_v(\eta)] < 0$. The two solutions will merge at the two turning points that delimit the locking band, which satisfy: $\cos[\phi + \alpha_v(\eta)] = 0$. In the sensing application, the input frequency is kept fixed at ω, so we will define the locking boundaries in terms of the parameter η. The two turning points that define the locking boundaries are denoted as η_{T1} and η_{T2}. They are given by

$$\begin{aligned} \omega &= \omega_o(\eta_{T1}) - B(\eta_{T1}) \\ \omega &= \omega_o(\eta_{T2}) + B(\eta_{T2}). \end{aligned} \tag{7}$$

Note that the magnitudes $|\omega - \omega_o(\eta_{Tm})|$, where $m = 1, 2$, must be small enough for the linearization (1) to be valid. Outside the locked-operation interval $\eta_{T1} < \eta < \eta_{T2}$, the system is governed by (2). If the free-running frequency ω_o decreases (increases) with η, the sensor should operate for $\eta > \eta_{T2}$ ($\eta < \eta_{T1}$). To derive the expression of the beat frequency (in unlocked conditions), we will apply the procedure in [26], [27], and [28] to the arbitrary oscillator considered in (1), described in terms of $Y(V, \omega) = Y_r(V, \omega) + jY_i(V, \omega)$. First, we integrate (2) with respect to time, which provides

$$\begin{aligned} &-\frac{B(\eta)}{\Delta\omega(\eta)} - \sqrt{1 - \left[\frac{B(\eta)}{\Delta\omega(\eta)}\right]^2} \tan\left(\xi(t - t_o)\right) \\ &\quad = \tan\frac{\left[\phi(t) + \alpha_v(\eta)\right]}{2} \end{aligned} \tag{8}$$

where $\xi = ((1/2)([\Delta\omega(\eta)]^2 - [B(\eta)]^2)^{1/2})$. Let us assume that there exists T such that $\phi(t+T) = \phi(t) + 2\pi, \forall t$. Then, we can write

$$\begin{aligned} &-\frac{B(\eta)}{\Delta\omega(\eta)} - \sqrt{1 - \left[\frac{B(\eta)}{\Delta\omega(\eta)}\right]^2} \tan\left(\xi(t + T - t_o)\right) \\ &\quad = \tan\frac{\left[\phi(t) + \alpha_v(\eta) + 2\pi\right]}{2} \\ &\quad = \tan\frac{\left[\phi(t) + \alpha_v(\eta)\right]}{2} \end{aligned} \tag{9}$$

where the property $\tan(\varphi + \pi) = \tan(\varphi), \forall\varphi$ has been applied. Now, comparing (8) and (9), the equality $\xi T = \pi$ is obtained, yielding

$$\begin{aligned} \omega_b &= \frac{2\pi}{T} \\ &= \sqrt{\left[\Delta\omega(\eta)\right]^2 - \left[B(\eta)\right]^2} = \sqrt{\left[\omega - \omega_o(\eta)\right]^2 - \left[B(\eta)\right]^2} \end{aligned} \tag{10}$$

where for better insight, we have introduced the explicit expression of $\Delta\omega(\eta)$. The beat frequency ω_b is zero at the two locking boundaries, η_{T1} and η_{T2}, and increases when moving away from the boundaries. The sensitivity of ω_b to the parameter η is given by

$$S_b = \frac{\partial\omega_b}{\partial\eta} = -\frac{\left[\omega - \omega_o(\eta)\right]\frac{\partial\omega_o(\eta)}{\partial\eta} + B(\eta)\frac{\partial B(\eta)}{\partial\eta}}{\omega_b(\eta)}. \tag{11}$$

From inspection, S_b is infinite at the two boundaries, which fulfill $\omega_b(\eta_{T1}) = 0$ and $\omega_b(\eta_{T2}) = 0$. Making use of the expression of ω_b, we can also write

$$S_b = \frac{\partial\omega_b}{\partial\eta} = -\frac{\frac{\partial\omega_o(\eta)}{\partial\eta} + \frac{1}{2\left[\omega - \omega_o(\eta)\right]}\frac{\partial\left[B(\eta)\right]^2}{\partial\eta}}{\sqrt{1 - \left(\frac{B(\eta)}{\omega - \omega_o(\eta)}\right)^2}}. \tag{12}$$

We will have a higher S_b for a smaller denominator. This implies similar values of $|\omega - \omega_o(\eta)|$ and $B(\eta)$, under the condition $|\omega - \omega_o(\eta)| > B(\eta)$. Thus, under a fixed ω_o, one way to expand the interval with sensitivity gain is to increase the locking bandwidth B. When doing so, we must ensure that the locking boundary still corresponds to a turning-point bifurcation, as in the case of Fig. 2(b). As discussed in Section II-A, when the unlocking mechanism corresponds to a turning point, the beat frequency exhibits high sensitivity to the parameter in the vicinity of the locking boundary. As also discussed, the sensitivity is lower in the case of unlocking through a Hopf bifurcation [see Fig. 2(c)].

As already stated, the targeted interval of the sensing parameter will depend on the particular application. Thus, one should be able to preset one of the locking boundaries (η_{T1} or η_{T2}), which can be done by properly selecting the input current amplitude I_g and frequency ω. The pairs ω and I_g that provide the same η_{T1} or η_{T2} are given by

$$\begin{aligned}\omega &= \omega_o(\eta_{T1}) - \frac{I_g}{V_o(\eta_{T1})}\frac{1}{\left|\frac{\partial Y_o(\eta_{T1})}{\partial \omega}\right|\sin\alpha_{v\omega}(\eta_{T1})}\\ \omega &= \omega_o(\eta_{T2}) + \frac{I_g}{V_o(\eta_{T2})}\frac{1}{\left|\frac{\partial Y_o(\eta_{T2})}{\partial \omega}\right|\sin\alpha_{v\omega}(\eta_{T2})}.\end{aligned} \tag{13}$$

Note that the above expressions require a previous calculation of the free-running solution $V_o(\eta_{Tm})$ and $\omega_o(\eta_{Tm})$, where $m = 1, 2$, and the derivatives of Y about this solution.

C. Oscillator Spectrum Outside the Locking Boundaries

The spectrum near the locking boundaries can be obtained by calculating the Fourier series of the voltage $v(t)$ at the analysis node

$$v(t) = 2\mathrm{Re}\left\{V(t)e^{j\omega t}e^{j(\phi(t)+\alpha_v)}\right\} \tag{14}$$

where $V(t)$ is the slowly varying oscillation amplitude in unlocked conditions. Following [28], we will express the complex exponential term in (14) as:

$$e^{j(\phi(t)+\alpha_v)} = \frac{1 + j\tan\frac{\phi(t)+\alpha_v}{2}}{1 - j\tan\frac{\phi(t)+\alpha_v}{2}}. \tag{15}$$

Because $B < |\Delta\omega|$, we can represent the quotient $(B/\Delta\omega)$ as the sinus of an angle variable θ, by defining $\sin\theta = -B(\eta)/\Delta\omega(\eta)$, where $-\pi/2 < \theta < \pi/2$. The variable θ relates B, $\Delta\omega$, and ω_b through a trigonometrical expression, which will enable an analytical calculation of the Fourier-series expansion of $e^{j(\phi(t)+\alpha_v)}$, in terms of θ and $\tan\theta$. Making use of (10), it is easily derived that $\omega_b = -\mathrm{sgn}(\Delta\omega)\Delta\omega\cos\theta$. Then, introducing (9) in (15) and setting $t_o = 0$, we obtain

$$\begin{aligned}e^{j(\phi(t)+\alpha_v)} &= \frac{\cos\frac{\omega_b t}{2} + j\sin\left(\frac{-\mathrm{sgn}(\Delta\omega)\omega_b t}{2} + \theta\right)}{\cos\frac{\omega_b t}{2} - j\sin\left(\frac{-\mathrm{sgn}(\Delta\omega)\omega_b t}{2} + \theta\right)}\\ &= \frac{1}{j\tan\frac{\theta}{2}}\left(\frac{1-\tan^2\frac{\theta}{2}}{1 - j\tan\frac{\theta}{2}e^{j(-\mathrm{sgn}(\Delta\omega)\omega_b t+\theta)}} - 1\right).\end{aligned} \tag{16}$$

Finally, the expansion of (16) in a Fourier series leads to

$$\begin{aligned}e^{j(\phi(t)+\alpha_v)} &= j\tan\frac{\theta}{2}\\ &\quad + \frac{1-\tan^2\frac{\theta}{2}}{j\tan\frac{\theta}{2}}\sum_{n=1}^{\infty}\left(j\tan\frac{\theta}{2}\right)^n e^{jn(\theta-\mathrm{sgn}(\Delta\omega)\omega_b t)}.\end{aligned} \tag{17}$$

Note that the frequency difference between consecutive spectral lines predicted by (17) is ω_b. When ω is above (below) the upper (lower) locking boundary, the harmonic components provided by (17) are located below (above) ω. Then, making $V(t) \cong V_o(\eta)$ in (14), the magnitude of the spectral lines is given by

$$\begin{aligned}U_0 &= V_o(\eta)\tan\frac{\theta}{2}\\ &\ldots\\ U_n &= V_o(\eta)\left(1-\tan^2\frac{\theta}{2}\right)\left(\tan\frac{\theta}{2}\right)^{n-1}\\ &= V_o(\eta)\left(1-\tan^2\frac{-B(\eta)/\Delta\omega(\eta)}{2}\right)\left(\tan\frac{-B(\eta)/\Delta\omega(\eta)}{2}\right)^{n-1}\end{aligned} \tag{18}$$

where U_0 is the node amplitude at the input frequency ω. Note that $B(\eta)/\Delta\omega(\eta) < 1$, so the tangent function is smaller than 1. In the logarithmic scale, the amplitude of the spectral lines $n \geq 1$ decreases linearly with n, as indicated in [28]. The spectral line at ω, with voltage amplitude U_0, evolves in a manner different from those at $n \geq 1$. As $\Delta\omega(\eta)$ increases, $\sin\theta$ and $\tan(\theta/2)$ decrease and the spectral line at $n = 1$ becomes dominant. The spectral lines at ω and $\omega + 2\mathrm{sgn}(\Delta\omega)\omega_b$ tend to exhibit the same amplitude, as observed in [28].

The frequency variation of a multiple n of ω_b for the same variation of the sensing parameter, η, is $n\omega_b$. Thus, at $n\omega_b$ the sensitivity increases from S_b to nS_b. Due to the amplitude decrease with n, the order must be limited to a relatively small value, such as 2 or 3. On the other hand, the amplitude V_0 of the spectral line at ω can constitute an additional sensing variable. Note that both U_0 and ω_b depend on $\Delta\omega$ and B, so there are two independent variables. This will provide a well-conditioned system to sense both the real and imaginary parts of the dielectric constant.

In Section III, we will address a cubic-nonlinearity oscillator at the fundamental frequency, where the above formulation leads to manageable analytical expressions, providing a detailed understanding of the sensor's performance. In contrast, the analysis of the transistor-based oscillator will rely on the semianalytical formulation, using numerical derivatives of the oscillator's admittance function, which is extracted from harmonic balance.

III. Cubic-Nonlinearity Oscillator

To get analytical insight, we will address the cubic-nonlinearity oscillator of Fig. 1(a), at the fundamental frequency, which will enable the derivation of analytical expressions. Note that for this analysis to be valid, the harmonic content must be sufficiently low. This condition is met with the passive element values provided in Fig. 1.

A. Analytical Calculation of the Beat Frequency and Locking Boundaries

In sensor applications [1], [2], [3], [4], [5], [6], [7], [8], the MUT often affects an equivalent capacitance, so here, we will take the capacitor C as the analysis parameter ($\eta = C$). For a given C, the free-running frequency ω_o and the bandwidth B (assuming a small I_g) are given by

$$\omega_o(C) = \frac{1}{\sqrt{LC}}$$
$$B(C) = \frac{I_g}{V_o}\frac{1}{\left|\frac{\partial Y_o}{\partial \omega}\right|\sin\alpha_{v\omega}} = \frac{I_g}{V_o}\frac{1}{2C}. \tag{19}$$

In view of the above expressions, under a constant input frequency ω and a low amplitude I_g, the locked-operation interval is centered about $C_o = 1/(L\omega^2)$ and its boundaries C_{T1} and C_{T2} fulfill

$$\omega = \sqrt{\frac{1}{LC_{T1}} - \frac{I_g}{V_o}\frac{1}{2C_{T1}}} \tag{20a}$$
$$\omega = \sqrt{\frac{1}{LC_{T2}} + \frac{I_g}{V_o}\frac{1}{2C_{T2}}}. \tag{20b}$$

Outside the locking band, the beat frequency ω_b varies with C as follows:

$$\omega_b = \sqrt{\left(\omega - \frac{1}{\sqrt{LC}}\right)^2 - \left(\frac{I_g}{V_o}\frac{1}{2C}\right)^2}. \tag{21}$$

As expected, at C_{T1} and C_{T2}, one obtains $\omega_b = 0$. Note that the above expression, which particularizes (10) to the circuit in Fig. 1(a), takes into account the effect of C on both the free-running frequency and the locking bandwidth.

As an example, we will consider the input frequency $f = 1.592$ GHz, input amplitude $I_g = 1$ mA, and inductor value $L = 4$ nH. The free-running amplitude is $V_o = ((-a-G)/(3b/4))^{1/2} = 1.547$ V, where a, b, and G are given in Fig. 1. Using (3)–(5), one obtains the locked-solution curve traced in blue in Fig. 3(a), in terms of the periodic-oscillation amplitude (right vertical axis). The analytical curve has been validated with HB, considering the fundamental frequency only, that is, using NH = 1, where NH denotes the number of harmonic terms. The periodic solutions have been calculated with the method in [21], which also provides the low-amplitude periodic curve. Note that, for this validation, the method in [21] has been limited to the fundamental frequency. As expected, the locked-solution curve is centered about $C_o = 1/(L\omega^2)$. The evolution of ω_b [calculated with (21)] versus C when moving away from the locking boundaries is also traced in Fig. 3(a), with its values shown in the left vertical axis. Note that the locked-operation interval fulfills $\omega_b = 0$, so it lies on the horizontal axis.

B. Detection of Beat Frequency From Envelope-Transient Simulations

Predictions by (22) have been validated with circuit-level envelope transient [30], [31]. The general representation of the voltage at the analysis node n is $v(t) = \sum_{p=-\mathrm{NH}}^{\mathrm{NH}} V_p(t)e^{jp\omega t}$,

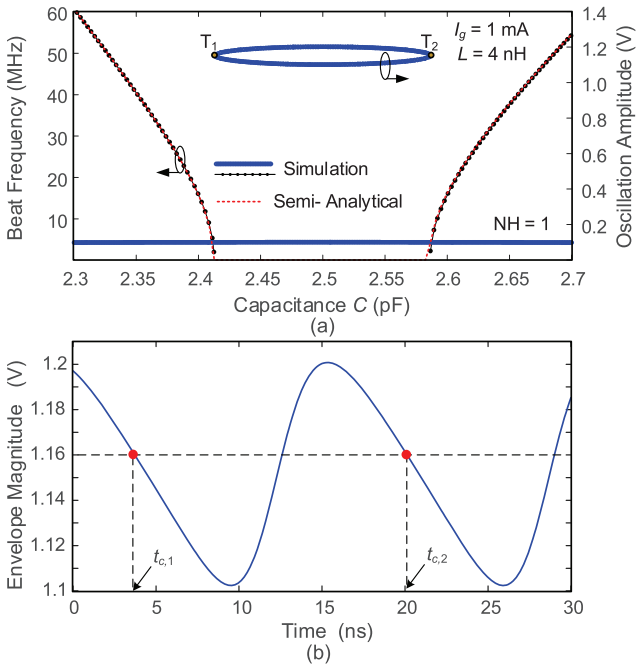

Fig. 3. Analysis of the oscillator in Fig. 1(a). (a) Periodic-solution curves and evolution of the beat frequency ω_b, calculated with (21) and with circuit-level envelope transient, using the method in Section II-D. There are two vertical axes. One is for the oscillation amplitude in locked conditions and the other is for the beat frequency in unlocked operation, as indicated by the arrows. (b) Beat-frequency detection for $C = 2.3$ pF. The signal $|V_1(t)|$ has been represented together with the samples $u_-(t_{c,j})$ for $j = 1, 2$, using $s = 1.16$ V.

where ω is the input frequency and $V_p(t)$ is the slowly varying harmonic term. When the oscillator reaches a locked state, the voltage phasors $V_p(t)$ become constant since the solution is periodic. When the oscillator is unlocked, the magnitude $|V_p(t)|$ exhibits, in a steady state, an oscillation at the beat frequency ω_b or the difference between the input frequency and the self-oscillation frequency. Note that the latter is affected by the input source and, thus, is different from the free-running one. The solution is quasi-periodic at the two fundamental frequencies ω (in the exponentials $e^{-jp\omega t}$ and $e^{jp\omega t}$) and ω_b [in the envelopes $V_{-p}(t)$ and $V_p(t)$]. The aim will be to detect ω_b from the evaluation of $V_1(t)$. Once the steady state is reached, this frequency can be calculated from the succession of time samples at which the waveform $u(t) = |V_1(t)|$ takes a particular value s, comprised in the excursion of $u(t)$. For the integration of the envelope-domain system, the time variable is discretized, so the waveform is constituted by the discrete time samples $u_k = |V_1(t_k)|$, where $t_k = (k-1)\Delta t$, $k = 1, \ldots, n$, and Δt is the time step [see Fig. 3(b)]. We will denote as $u_+(t_{c,j})$ or $u_-(t_{c,j})$, where $j = 1$ to m, the sequence of $u(t)$ values that cross the straight line $u(t) = s$ with positive or negative slope, respectively. Mathematically, these two sequences are defined by the two following conditions:

$$\operatorname{sgn}(u_k - s)\cdot\operatorname{sgn}\left(u_{k+1} - s\right) < 0$$
$$\operatorname{sgn}\left(u_{k+1} - u_k\right) = \pm 1. \tag{22}$$

Once we have either $u_+(t_{c,j})$ [corresponding to +1 in 20(b)] or $u_-(t_{c,j})$ [corresponding to −1 in 20(a)], the beat frequency

is approached as the average $\omega_b \simeq 2\pi/T_b$, where

$$T_b = \sum_{j=1}^{m-1} \left(t_{c,j+1} - t_{c,j}\right)/(m-1) = \left(t_{c,m} - t_{c,1}\right)/(m-1). \quad (23)$$

The results obtained with the above procedure have been represented in Fig. 3(a) and are overlapped with the analytical calculations.

C. Sensitivity Analysis

Next, we will analyze the impact of two parameters: the inductor L and the input amplitude I_g. Under the usual case of an increase in C under the MUT variations, there will be a reduction of ω_o. Because the oscillator must be unlocked in the full sensing interval, we will set the upper boundary C_{T2}. For each L or I_g, we will calculate the required input frequency ω from 20(b). Introducing (19) and 20(b) into (12), we obtain the following expression for the sensitivity of ω_b with respect to C:

$$S_b = \frac{\frac{L}{(LC)^{3/2}} + \frac{1}{2\Delta\omega_2}\frac{I_g^2}{V_o C^3}}{2\sqrt{1-\left(\frac{I_g}{2CV_o\Delta\omega_2}\right)^2}} \quad (24)$$

where

$$\Delta\omega_2 = \frac{I_g}{V_o}\frac{1}{2C_{T2}} - \frac{1}{\sqrt{L}}\left(\frac{1}{\sqrt{C}} - \frac{1}{\sqrt{C_{T2}}}\right). \quad (25)$$

We will initially consider variations in L. Under the same values of I_g, V_o, and C, a smaller L increases the magnitude of the numerator and reduces that of the denominator, leading to higher sensitivity. This is verified in Fig. 4(a) by setting C_{T2} = 2.58 pF. The input current amplitude is I_g = 1 mA and the free-running oscillation amplitude is V_o = 1.547 V. Note that the locked-operation interval fulfills ω_b = 0, so it lies on the horizontal axis. As can be observed, the sensitivity is higher for smaller L. The predictions by (21) have been validated with envelope-transient simulations considering NH = 1 and making use of (23) to calculate the beat frequency. They are overlapped in all cases. In Fig. 4(b), the sensitivity of the beat frequency ω_b is compared with that of the free-running frequency ω_o for two different pairs of values (L, ω). Note that we have made the subtraction $\omega - \omega_o$ to have comparable magnitudes. The sensitivity of ω_b is higher than that of the free-running frequency (for the same two L values), consistent with the findings of [18]. The comparison also demonstrates that the higher sensitivity of ω_b is maintained over a sufficiently large parameter interval. Remember that we intend to sense small parameter variations. In Fig. 4(c), we compare the spectra obtained for the same increment of C (given by: ΔC = 0.02 pF) and two different L's. The spectra are composed of multiple spectral lines, spaced by ω_b. They have been calculated using (18), represented with circles, and circuit-level envelope transient with NH =1. As can be seen, there is a very good agreement. Discrepancies are attributed to the assumption of a constant amplitude $V(t) \cong V_o$ in (18). The improvement of sensitivity at $n\omega_b$ is evident from Fig. 4(c) and agrees with previous discussions. Care must be taken to avoid an integer value n for which the amplitude of the spectral line is too low.

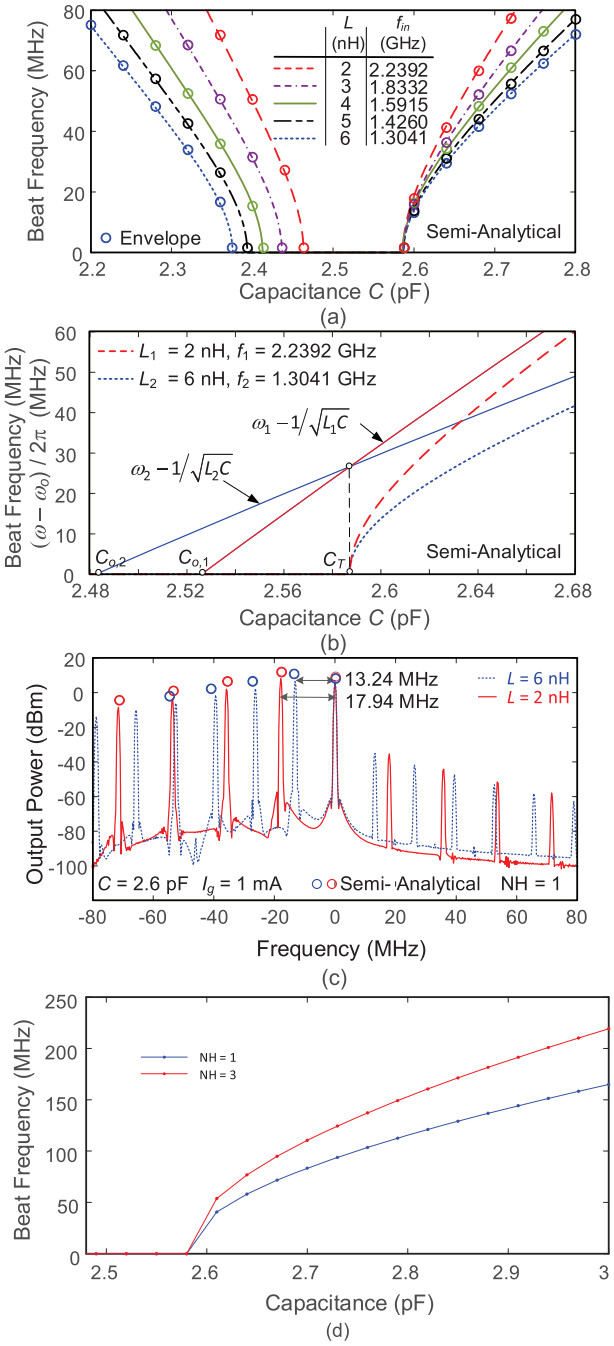

Fig. 4. Analysis of the oscillator in Fig. 1(b). Influence of the inductor L. (a) Sensitivity of the beat frequency ω_b for different values of L. The upper locking boundary is maintained at C_{T2} = 2.58 pF. The results are validated with envelope transient considering NH =1. (b) Comparison of the variation of ω_b with that of $\omega - \omega_o$. (c) Spectra obtained under the same increment of C (given by: ΔC = 0.02 pF) for two different L values. Calculations with (18), represented with circles, are compared with envelope transient, considering NH =1. (d) Variation of the beat frequency ω_b versus the capacitor C when considering NH =1 and NH =3, for L = 5.3 nH.

Under a fixed ω_o, without modifying the original design, we can improve the sensitivity by increasing the input amplitude I_g, which gives rise to a larger bandwidth B, as seen in (19). A

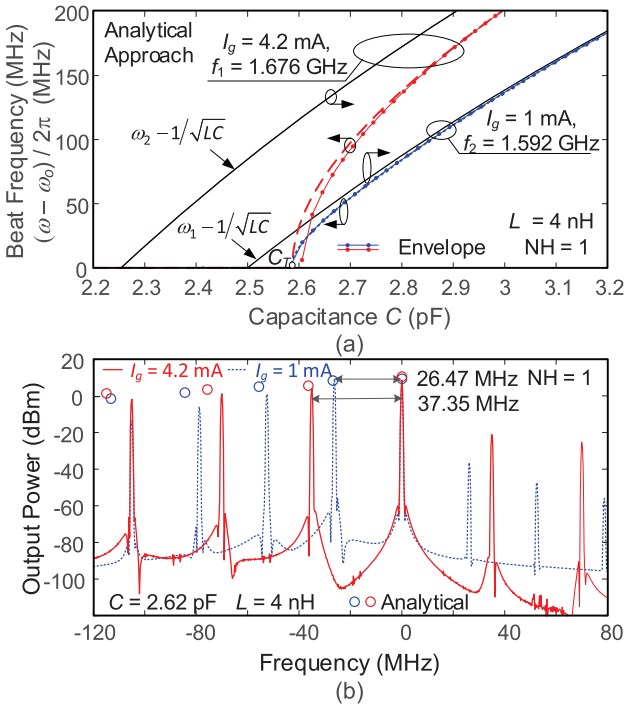

Fig. 5. Influence of the input amplitude I_g. (a) Sensitivity enhancement when increasing I_g from 1 to 4.2 mA while maintaining the upper locking boundary at C_{T2} = 2.58 pF. The variation of ω_b is compared to that of $\omega - \omega_o$. (b) Spectra obtained, for the two I_g values, under the same increment of C, given by: ΔC = 0.02 pF. They have been calculated using (18), represented with circles, and envelope transient, considering NH =1.

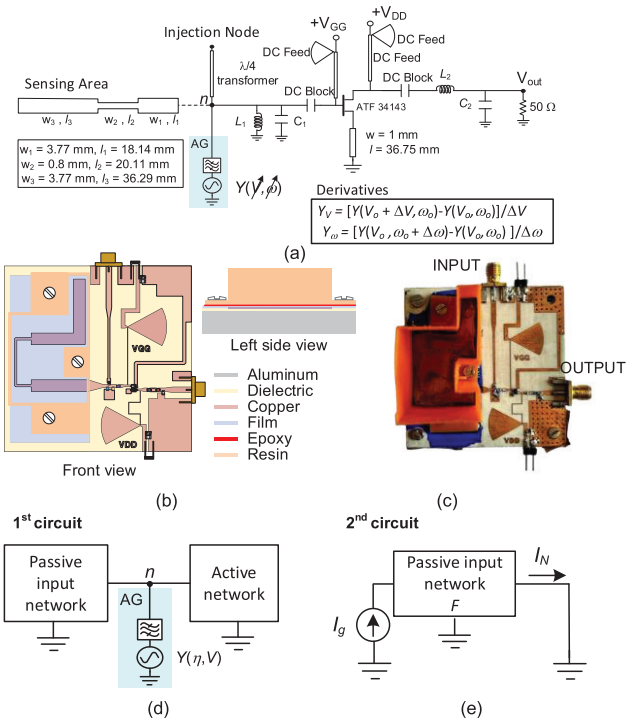

Fig. 6. Sensor implemented with a transistor-based oscillator. (a) Schematic. The AG is introduced to calculate the derivatives through finite differences. The arrows indicate the two consecutive variable sweeps. (b) Layout for liquid sensing. A left-side view with the resin holder sealed with epoxy glue and screws on a polyethylene terephthalate (PET) film is shown. (c) Photograph. (d) and (e) Simulation setup to obtain the injection-locked curves. Oscillator in the absence of the injection source [in (d)] and input network in the presence of this source [in (e)].

higher I_g increases the magnitude of the numerator of (24) and reduces that of the denominator, leading to higher sensitivity.

Fig. 5(a) shows the improvement of sensitivity when increasing I_g from 1 to 4.2 mA. The variation of $\omega - \omega_o$ versus C is also shown. The beat frequency ω_b is significantly more sensitive. Note that for I_g = 4.2 mA, there is a slight discrepancy between the upper locking boundary C_{T2} obtained with (20) and with envelope transient. This is because, under a higher input amplitude, the locked-solution curve deviates from the perfect ellipse resulting from the approximation (5). This problem will be fully solved with the HB-based method presented in Section IV. The new method will allow setting the upper or lower locking boundary for arbitrary shapes of the locked-solution curves, in the presence of multiple harmonic terms. The spectra in Fig. 5(b) enable the comparison of the beat frequency obtained for I_g = 1 mA and I_g = 4.2 mA under the same capacitor increment ΔC = 0.02 pF. The increment of ω_b is about twice the one obtained when varying L [see Fig. 5(b)]. The analytical results of (18) (represented with circles) have been validated through their comparison with the numerical spectra of Fig. 5(b), obtained with circuit-level envelope transient. As expected, accuracy decreases when increasing the driving amplitude I_g, because the linearization considered in (1) becomes less accurate.

It is relevant to note that when considering NH =3, the oscillator admittance has the general expression $Y(V, \omega) = Y_r(V, \omega) + jY_i(V, \omega)$. Then, all the components in expression (4) of the bandwidth B, including the amplitude V_o and the angle $\alpha_{v\omega}$, depend on the sensing parameter. In this particular case, this gives rise to an increase in sensitivity, as shown in Fig. 4(c).

IV. Methodology Based on Harmonic Balance

In this section, we apply the semianalytical formulation from Section II to the transistor-based oscillator in Fig. 6. While this method provides valuable insights into performance, it may have limitations in accuracy. To overcome these limitations, we will introduce a new method that allows precise setting of either the upper or lower locking boundary to match the expected variation range of the sensing parameter.

A. Application of the Semianalytical Method

The sensor oscillator in Fig. 6 is based on a PHEMT transistor ATF34143 and is manufactured on Rogers 4003C, with ε_r = 3.55 and h = 32 mil. It is a single-ended oscillator design, having a transmission line as a series feedback element. The 50-Ω load enables the extraction of an output signal for the experimental characterization. The inductor L_2 and capacitor C_2 are tuned to obtain negative resistance at the gate terminal. In turn, the resonance condition is achieved with the network connected to the gate terminal, considering the imaginary part of the admittance seen from the transistor's gate terminal. This network includes the stepped-impedance resonator and an LC network (L_1 and C_1), which prevents oscillations at higher resonance frequencies of the stepped-impedance resonator.

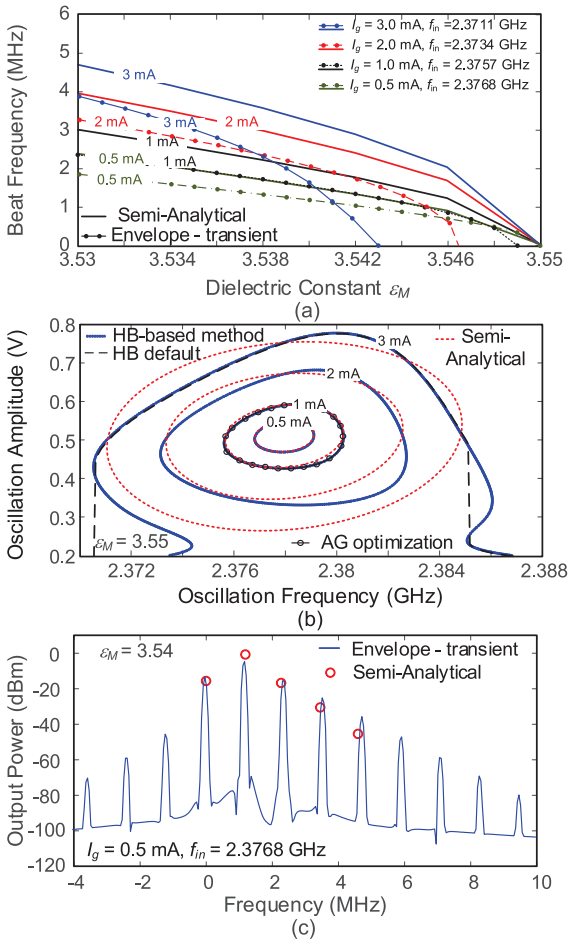

Fig. 7. Semianalytical method applied to the transistor-based oscillator. (a) Variation of the beat frequency ω_b for $\varepsilon_{M,T1} = 3.55$ and four different pairs (ω, I_g), having $I_g = 0.5$, 1, 2, and 3 mA and ω calculated with (13). The results are compared with those obtained with circuit-level envelope transient and (18). (b) Comparison of the locked-solution curves versus ω obtained through (3) and (5), for $\varepsilon_M = 3.55$ and the same four I_g values, with those obtained with the HB-based method in [21]. The open solution curve obtained for $f = 2.370$ GHz and $I_g = 3$ mA is validated with commercial harmonic balance, unable to circumvent the turning points. (c) Comparison of the unlocked spectrum obtained for $I_g = 0.5$ mA, $f = 2.3768$ GHz, and ε_M with the semianalytical expressions (18) and with circuit-level envelope-transient simulations.

The high-slope resonance of this resonator has the greatest influence on the oscillation frequency. In this type of resonator, sections with high and low characteristic impedances alternate. We have considered $Z_H = 120\ \Omega$ and $Z_L = 30\ \Omega$. In the case of an odd number of sections, as in the circuit of Fig. 6, the electrical length of the outermost section is π, with a low characteristic impedance at the desired resonance frequency, $f_r = 2.4$ GHz. The electrical lengths of the other sections are $\pi/2$ at f_r [1], [14]. In the absence of the MUT, the free-running oscillation frequency is $f_o = 2.42$ GHz. The MUT is placed over the stepped-impedance resonator. The MUT dielectric constant is ε_M, which will be varied within a small interval below $\varepsilon_M = 3.55$. Thus, ε_M plays the role of the parameter η. Because the oscillation frequency increases when reducing ε_M, the selected locking boundary will be the lower one, so we will set $\eta_{T1} = \varepsilon_M$ and $_{T1} = 3.55$.

To apply the method in Section II, we must calculate the derivatives of an admittance function $Y(V, \omega)$ about the free-running solution obtained for each $\varepsilon_M < 3.55$. For this calculation, we will introduce a voltage-type auxiliary generator (AG) [37], [39] in parallel at the analysis node n. In the circuit of Fig. 6(a), this node corresponds to the gate terminal. The AG has amplitude V and frequency ω. We first obtain the free-running solution $V_o(\varepsilon_M)$ and $\omega_o(\varepsilon_M)$ (with NH =7 harmonic terms) and then apply finite differences with respect to V and ω to numerically calculate the derivatives $\partial Y_o(\varepsilon_M)/\partial V$ and $\partial Y_o(\varepsilon_M)/\partial\omega$ [37], [39], considering NH harmonic terms [see Fig. 6(a)]. For each ε_M, these derivatives are calculated at $V_o(\varepsilon_M)$ and $\omega_o(\varepsilon_M)$ by doing

$$\begin{aligned}\frac{\partial Y_o(\varepsilon_M)}{\partial V} &= \frac{Y(V_o+\Delta V,\omega_o)-Y(V_o,\omega_o)}{\Delta V}\\ &= \frac{Y(V_o+\Delta V,\omega_o)}{\Delta V}\\ \frac{\partial Y_o(\varepsilon_M)}{\partial \omega} &= \frac{Y(V_o,\omega_o+\Delta\omega)-Y(V_o,\omega_o)}{\Delta\omega}\\ &= \frac{Y(V_o,\omega_o+\Delta\omega)}{\Delta\omega}\end{aligned} \tag{26}$$

where ΔV and $\Delta\omega$ are small increments, which must be large enough to ensure sensitivity of the HB simulation and small enough to ensure a linear response of Y about $V_o(\varepsilon_M)$ and $\omega_o(\varepsilon_M)$. As an example, for $\varepsilon_M = 3.55$, we have

$$\begin{aligned}&\partial Y(V_o,\omega_o)/\partial V\\ &\quad = (2.37917\times10^{-2} - j4.3188\times10^{-3})\Omega^{-1}/V\\ &\partial Y(V_o,\omega_o)/\partial\omega\\ &\quad = (7.34176\times10^{-12} + j1.36818\times10^{-10})\Omega^{-1}s.\end{aligned} \tag{27}$$

To set the lower locking boundary at $\eta_{T1} = \varepsilon_M$ and $_{T1} = 3.55$, we will apply (13) considering four different input amplitudes: $I_g = 0.5$, 1, 2, and 3 mA. For each of the four resulting pairs (ω, I_g), we obtain the beat frequency ω_b versus ε_M using (10), which provides the curves in Fig. 7(a). This requires the calculation of the sequence of numerical derivatives of $Y(V, \omega)$ about the sequence of free-running points $[V_o(\varepsilon_M), \omega_o(\varepsilon_M)]$, obtained versus the parameter ε_M. As expected, in all cases, we obtain the same lower locking boundary $\varepsilon_{M,T1} = 3.55$. In the same figure, we compare the semianalytical prediction of the beat frequency ω_b with the one obtained through circuit-level envelope transient and (23). For the lower I_g values, the curves overlap near the locking boundary $\varepsilon_{M,T1} = 3.55$. The semianalytical formulation accurately predicts this boundary for $I_g = 0.5$ mA. However, as I_g increases, the circuit-level envelope-transient analysis predicts $\omega_b = 0$ (locking boundary) at progressively lower ε_M. This discrepancy, as well as the degradation in the prediction of ω_b, can be attributed to the failure of the linearization with respect to the frequency ω. To illustrate this, Fig. 7(b) compares the locked-solution curves versus ω obtained through (3)–(5) for $\varepsilon_M = 3.55$ with those obtained with the HB-based method in [21] (summarized in Section IV-B). The free-running solution, with frequency: $f_o = 2.378$ GHz and voltage amplitude $V_o = 0.509$ V, agrees with the center of the perfect ellipses that are obtained for small input amplitude, as easily derived from (3) to (5). Commercial HB converges by default to the low-amplitude curves, missing

the closed ones. As I_g increases, there is a significant deviation from the perfect ellipse predicted by (3)–(5). Of course, (3) and (5) are totally unable to predict the curve merging, in the same manner as the less realistic approaches [26], [27], [28]. Note that, for $I_g = 3$ mA, this merging has already taken place. The resulting open solution curve is validated with commercial harmonic balance, unable to circumvent the turning points. Thus, a methodology with general applicability is needed, which will be presented in Section III. However, for low I_g, we can expect a good prediction capability of the circuit behavior. This is shown in Fig. 7(c), which presents the unlocked spectrum for $I_g = 0.5$ mA, $f = 2.3768$ GHz, and ε_M. The results of the semianalytical expressions (18) are successfully compared with those obtained with circuit-level envelope-transient simulations.

B. Solution Curves in Injection-Locked Conditions [21]

In this section, we will summarize the method to obtain the locked-solution curves versus a given parameter ρ. Note that this parameter is a general one with respect to which the injection-locked-solution curve will be calculated. It does not necessarily agree with the sensing parameter η. We must emphasize that commercial HB does not provide injection-locked solutions by default. To obtain the locked-solution curves, we will carry out a simultaneous simulation of two circuits [21]: the oscillator in the absence of the injection source [see Fig. 6(d)] and the input network in the presence of this source [see Fig. 6(e)]. The first one is used to obtain the oscillator nonlinear admittance function Y at the selected analysis node, calculated with NH harmonic terms. With this aim, a voltage AG with amplitude V is connected in parallel to the analysis node n. We will perform a double sweep in the parameter ρ and the AG amplitude V. At each sweep step, we perform an HB simulation with NH harmonics and calculate Y as the ratio between the AG current and the voltage V.

The second (simultaneous) analysis addresses the input network [see Fig. 6(e)] defined between the driving source and the analysis node n. The aim is to obtain the linear function $F(\rho)$ that relates Norton's equivalent current to the input source. Assuming a current input source, I_g, we will have: $I_N = F(\rho)I_g$. The periodic-solution curve(s) is described with

$$H(\rho, V) = \frac{Y(\rho, V)}{F(\rho)} V = I_g e^{-j\phi} \tag{28}$$

where ϕ is the phase shift between V at the analysis node and the input source. For each I_g, the periodic-solution curves (in terms of V) are given by the constant-amplitude contour(s) $|H| = I_g$. The above method was applied to obtain the solution curves versus $\rho = \omega$, as shown in Fig. 7(b). In the circuit of Fig. 6, $F = 1$. The method has been validated through AG optimization [37] for the case $I_g = 1$ mA.

C. New Method to Set the Locking Boundaries

As already discussed, the increase in sensitivity should be obtained without altering the selected locking boundary, η_{T1} or η_{T2}. However, the semianalytical method in Section II is only accurate for lower values of the input amplitude, due to the deviation of the locked-solution curve from a perfect ellipse. To address this issue, we will present a general method that utilizes the mathematical condition satisfied at turning-point bifurcations. At these points, the Jacobian matrix of the steady-state equation system becomes singular, consistent with the infinite slope. To derive the mathematical condition, we will make $\rho = \eta$ in (28). The Jacobian matrix is obtained by splitting (28) into real and imaginary parts, which provides the following singularity condition, to be fulfilled at the desired boundary η_T:

$$\det\left[H(\eta_T, V)\right] = \det\begin{bmatrix} \dfrac{\partial H^r(\eta_T, V)}{\partial \eta} & \dfrac{\partial H^r(\eta_T, V)}{\partial V} \\ \dfrac{\partial H^i(\eta_T, V)}{\partial \eta} & \dfrac{\partial H^i(\eta_T, V)}{\partial V} \end{bmatrix} = 0. \tag{29}$$

Considering the equality $H(\eta, V) = I_g e^{-j\phi}$, it is straightforward to derive

$$\det\left[H(\eta_T, V)\right] = \frac{\partial |H(\eta_T, V)|^2}{\partial V} = 0. \tag{30}$$

The aim is to maximize the sensitivity by tuning an additional parameter μ, as well as the input amplitude I_g. In the procedure, we will impose $\eta = \eta_T$ and perform a double sweep in $\rho = \mu$ and the excitation amplitude V. Note that the parameter $\rho = \mu$ is an auxiliary one, with respect to which the locked-solution curves will be traced. The set of μ and V values that provide the same locking boundary $\eta = \eta_T$ is given by the condition

$$\det\left[H(\mu, V, \eta_T)\right] = 0. \tag{31}$$

Note that for each pair of values (μ, V) fulfilling (31), we should have a different input amplitude I_g, given by (28). The curve (31) is easily obtained as the zero-value contour of the determinant function det. The pairs (I_g, μ) that provide the same η_T are given by the intersections of the curves (28) (with $\rho = \mu$) and (31).

As shown in Section II, the sensitivity increases with the bandwidth B. Without modifying the design, this bandwidth is broader for a higher input amplitude I_g, if the amplitude does not reach excessively high values. This is not an issue since those high values must be avoided as they will lead to unlocking through secondary Hopf bifurcations (instead of the desired local-global turning-point bifurcations). The additional parameter considered will be the input frequency, so we will have $\rho = \mu = \omega$. We will set $\varepsilon_{M,T} = 3.55$ and will carry out a double sweep in $\mu = \omega$ and V, performing an HB simulation (with NH =7) of the two circuits in Fig. 6 at each sweep step. Next, we will obtain the function $H(\omega, V)$ [see (28)] and the following zero-value contour:

$$\det\left[H(\omega, V)\right] = \frac{\partial |H(\omega, V)|^2}{\partial V} = 0. \tag{32}$$

As stated, the pairs (ω, I_g) that provide the same locking boundary $\varepsilon_{M,T} = 3.55$ are given by the intersections of the turning-point locus $\det[H(\omega, V)] = 0$ with the constant-amplitude contours $|H(\omega, V)| = I_g$. The results are shown in Fig. 8(a). For intersections on the left-hand side (right-hand side), $\varepsilon_{M,T} = 3.55$ will be the lower (upper) boundary. As

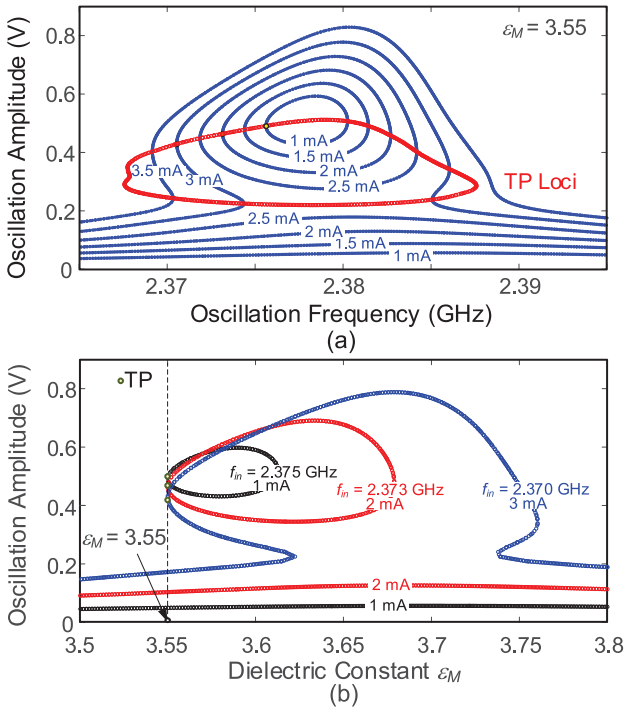

Fig. 8. Procedure to set the boundaries of the locking band. (a) Family of periodic-solution curves versus the input frequency ω when setting $\varepsilon_M = \varepsilon_{M,T} = 3.55$. The pairs (ω, I_g) that provide the locking boundary $\varepsilon_{M,T} = 3.55$ are given by the intersections of the turning-point locus (in red) and the constant-amplitude contours $|H| = I_g$. (b) Periodic-solution curves versus ε_M. We have selected three intersection points (ω, I_g), corresponding to the lower locking boundary. All of them exhibit a lower turning point at $\varepsilon_{M,T} = 3.55$.

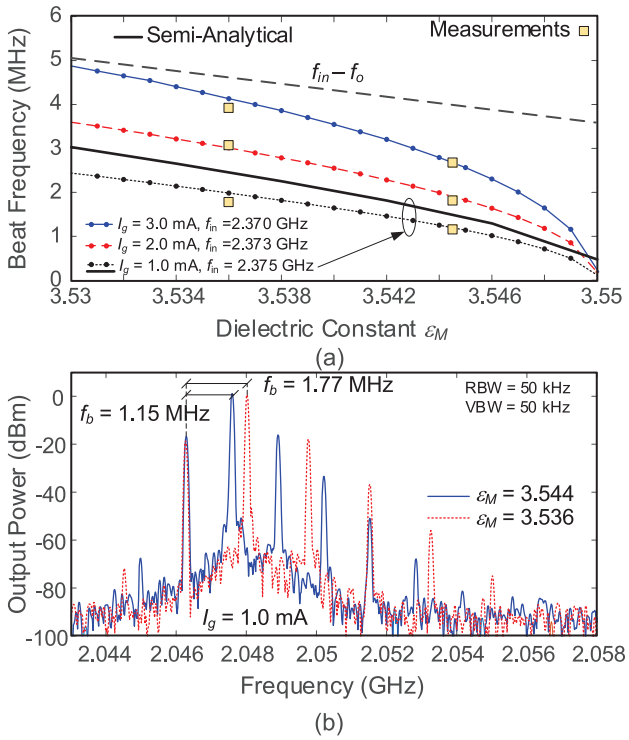

Fig. 9. Oscillator in unlocked conditions. (a) Variation of the beat frequency ω_b obtained by applying (18) to the waveforms resulting from circuit-level envelope transient. We have considered the same three pairs (ω, I_g) of Fig. 8(b). When reducing ε_M from $\varepsilon_{M,T} = 3.55$, the beat frequency starts from zero in the three cases. The results obtained with the analytical expression (9), using numerical derivatives of the AG admittance Y are also plotted. Measurements carried out with Rogers 4003C substrate with holes drilled are superimposed. (b) Spectra measured for $I_g = 1$ mA and the two estimated values $\varepsilon_{M,\text{eff}} = 3.536$ and $\varepsilon_{M,\text{eff}} = 3.544$.

stated, our goal is to set the lower boundary, so we have selected pairs (ω, I_g) on the left-hand side. The accuracy of the procedure is validated in Fig. 8(b), where we have traced the periodic-solution curves versus ε_M, for three pairs (ω, I_g). Note that to obtain the curves in Fig. 8(b), we have calculated the constant-amplitude contours of (28) with $\rho = \eta$. The three solution curves exhibit a turning point at the imposed lower boundary $\varepsilon_{M,T} = 3.55$. Note that the amplitude V at the turning point is different in the three cases, which does not affect the accuracy of the boundary.

To validate this new method, we have analyzed the oscillator in Fig. 6 with circuit-level envelope transient, using (18) to detect the beat frequency ω_b. We have considered NH =7 harmonic terms for consistency with the HB-based method. Note that the two analysis methods are independent. When taking the same three pairs (ω, I_g) of Fig. 8(b), we obtain the results in Fig. 9(a). When reducing ε_M from $\varepsilon_{M,T} = 3.55$, the beat frequency starts from zero in the three cases, which further demonstrates the accuracy. In agreement with the theoretical study of Section II, the sensitivity increases with I_g, due to the associated increase of the locking bandwidth B. As stated, the objective of this work is to demonstrate new analysis and simulation methods to enhance sensitivity near the locking boundaries, rather than achieving record sensitivity, which would depend on the original oscillator design.

In Fig. 9(a), we have also represented the variation of ω_b versus ε_M obtained with the analytical expression (9), for $I_g = 1$ mA, which is traced in solid green. As already shown in Fig. 7(a), there is a significant deviation with respect to circuit-level envelope transient.

D. Experimental Results

The sensor has been experimentally characterized using the system in Fig. 10. The output port of the sensor is connected to the R&S FSWP8 phase-noise analyzer to display both the output and phase-noise spectra. The drain and gate ports are biased using the low-noise internal sources of the analyzer. An Anritsu MG3710A Vector Signal Generator is used to generate the injection signal. The MUT samples cover the stepped-impedance resonator and are fixed to the printed circuit board (PCB) with nylon screws. To produce the small variations of ε_M considered in Fig. 9, holes have been uniformly drilled and distributed in the substrate, as proposed in [40] and [41]. Following [42] and [43], the effective ε_M is calculated with:

$$\varepsilon_{M,\text{eff}} = \varepsilon_M \frac{1 + 2V_F \frac{1-\varepsilon_M}{1+2\varepsilon_M}}{1 - V_F \frac{1-\varepsilon_M}{1+2\varepsilon_M}} \tag{33}$$

where V_F is the volumetric fraction of air in the material, which changes with the radium and/or number of holes. As shown in Fig. 9(a), the measurements show excellent

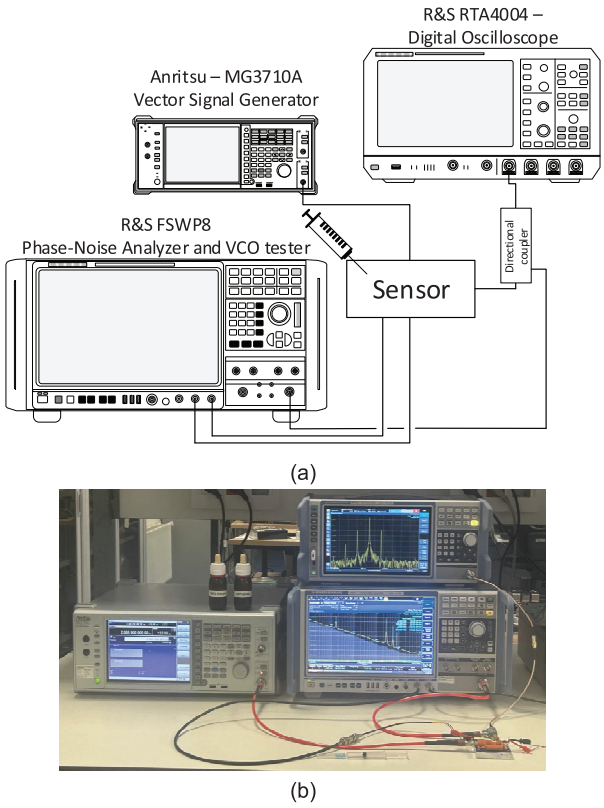

Fig. 10. Measurement setup. The output port of the sensor is connected to the R&S FSWP8 phase-noise analyzer to display both the output and phase-noise spectra. (a) Schematic. (b) Photograph.

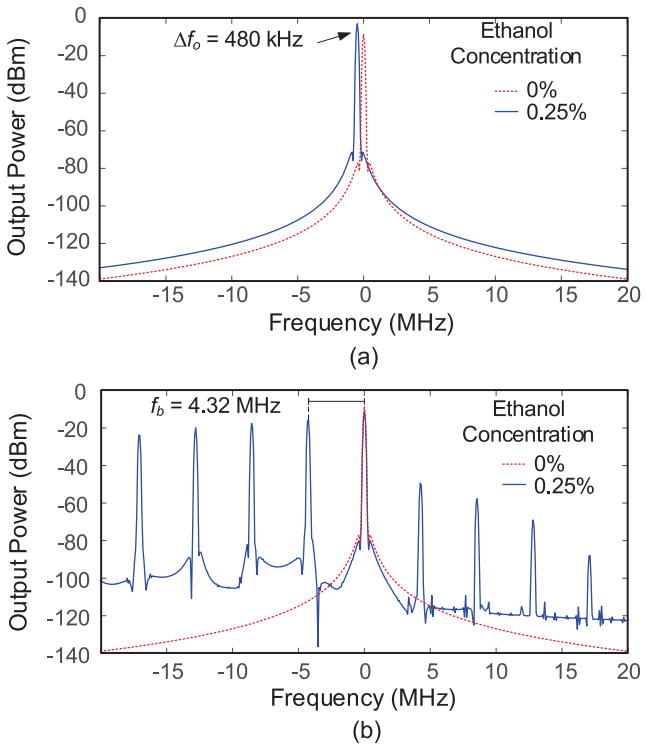

Fig. 11. Envelope-transient simulation of the transistor-based oscillator with NH =7 harmonic terms. We have used an experimental description of the stepped-impedance resonator with the deposit over it. (a) Variation of the free-running frequency when adding one drop of ethanol to the water volume. (b) Variation of the beat frequency for the same experiment.

TABLE I
SENSITIVITY COMPARISON

	$\Delta\varepsilon_M$	Δf(MHz)	Resonance frequency (GHz)	MUT
[44]	0.02	3	4.62	Dielectric substrate
[45]	0.11	0.2	2.18	Dielectric substrate
[46]	0.02	2.66	5.95	Dielectric substrate
[47]	0.02	3.3	2.47	Dielectric substrate
This work	**0.02**	**4.8**	**2.45**	Dielectric substrate

agreement with the analysis results. The spectra measured for the two estimated values $\varepsilon_{M,\text{eff}} = 3.536$ and $\varepsilon_{M,\text{eff}} = 3.544$ are shown in Fig. 9(b). The experimental shift of the beat frequency is 0.62 MHz, whereas in simulation, it is 0.7 MHz. The experimental shift of the free-running frequency is 0.16 MHz, whereas in simulation, it is 0.29 MHz. Thus, there is good qualitative agreement. The sensitivity could be improved with a more sensitive free-running oscillator design, as the beat-frequency sensor provides a sensitivity gain compared to free-running conditions. Nevertheless, in Table I, we compare our results with those of sensors based on the variation of the resonance frequency, when considering defective substrates.

We have also evaluated the capability to sense liquid mixtures. To achieve this, a ultraviolet (UV)-sensitive resin holder was designed and fabricated using a 3-D printer. The holder ensures that the liquid is contained over the sensing area. To prevent potential absorption by the substrate, the sensing surface is first laminated with a PET film with a thickness of 25 μm [48], [49]. The holder is positioned so that it does not rest on the microstrip lines responsible for sensing the liquid. To ensure a proper seal, the holder is glued to the PCB using a two-component epoxy adhesive and further secured with nylon screws. A resin holder has been made with a 3-D printer and sealed with epoxy glue and screws. To avoid possible absorption by the substrate, a PET film was placed over the sensing area [see Fig. 6(c)]. We have added drops of ethanol, with dielectric constant $\varepsilon_r = 24.3$, to a volume of 5 mL of DI water, with dielectric constant $\varepsilon_r = 80$. Each drop has a volume of 0.0125 mL. The added drops should slightly increase the effective dielectric constant ε_M of the total volume.

To accurately predict the variation of the beat frequency ω_b in simulation, we have experimentally characterized the scattering parameter S_{11} of the stepped-impedance resonator with the deposit over it when adding one to seven drops. The measured parameter S_{11} is introduced in the circuit (replacing the stepped-impedance resonator), and envelope-transient simulations with NH =7 are performed. Under injected conditions, the input frequency is set to $f = 2.086$ GHz, with the input power –28 dBm. When adding just one drop, the free-running frequency ω_o and the beat frequency ω_b undergo the shifts shown in Fig. 11. As can be seen, f_o varies 480 kHz, whereas f_b varies 4.32 MHz. Fig. 12 presents the experimental results. There are slight discrepancies between measurements and simulations, attributed to modeling inaccuracies and tolerances

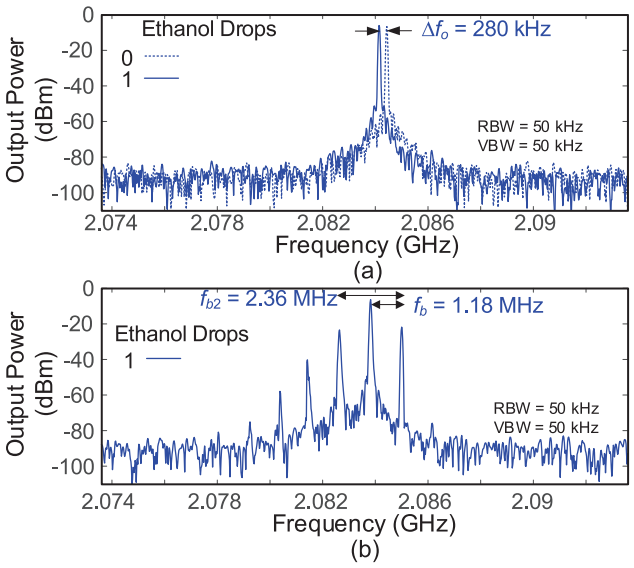

Fig. 12. Experimental results. (a) Variation of the free-running frequency when adding one drop of ethanol of 0.0125 mL to a water volume of 5 mL. (b) Variation of the beat frequency for the same experiment.

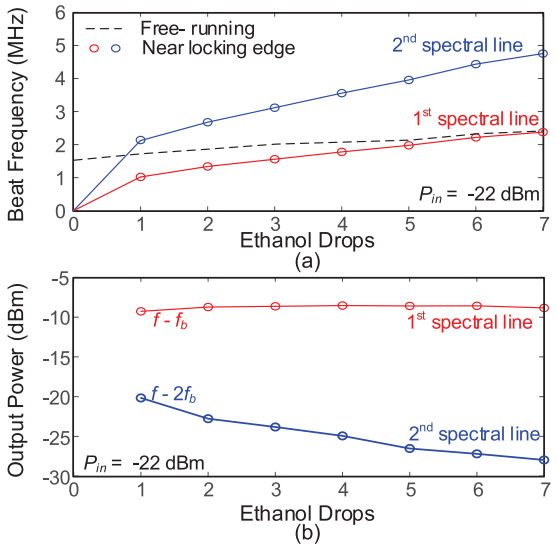

Fig. 13. Experimental validation of the sensing capabilities. (a) Variation of ω_b and $2\omega_b$ with the number of ethanol drops of 0.0125 mL in 5 mL of DI water. (b) Variation of output power at ω–ω_b and $\omega - 2\omega_b$.

in the active device. To estimate the variation of the dielectric constant, we will consider: $\varepsilon_w = 80 + j8$, for DI water, and $\varepsilon_{\text{eth}} = 8 + j8$, for ethanol, as provided in [50] and other sources while accounting for the volumetric concentrations. By adding one drop of ethanol, the dielectric constant decreases from $\varepsilon_M = 80 + j8$ to $\varepsilon_M = 79.8 + j7.99$.

Fig. 13(a) shows the variation of ω_b and $2\omega_b$ with the number of ethanol drops. The results demonstrate the possibility to sense at higher multiples of ω_b, thereby increasing the sensitivity. Clearly, sensing at $2\omega_b$ doubles the sensitivity. We have also represented the difference $f - f_o$, to further demonstrate the higher sensitivity of the beat frequency. Remember that $f = 2.086$ GHz. The frequency increment $\Delta\omega$ increases with the number of ethanol drops. Thus, according to (18), the power at the spectral line at $\omega - \omega_b$ should increase and the power at $\omega - 2\omega_b$ should decrease, as experimentally verified in Fig. 13(b). Using both the beat frequency and output power, it should be possible to obtain the real and imaginary parts of the dielectric constant, after a suitable calibration. The procedure would be analogous to the one in [14] and [21], so it is not presented here.

V. Phase-Noise Analysis

In this section, we will investigate, for the first time to our knowledge, the oscillator phase noise when it is unlocked and operating close to a turning-point local-global bifurcation. In the unlocked oscillator, we will have two incommensurable fundamental frequencies ω and ω_b. Since the time dependence of the amplitude and phase components in (14) is due to the beat frequency ω_b, these components can be expressed as follows:

$$V(t) = V_0(\eta) + \sum_{k=-\infty}^{\infty} \Delta V_k e^{jk\omega_b t}$$
$$\phi(t) = -sgn(\Delta\omega)\omega_b t + \sum_{k=-\infty}^{\infty} \Phi_k e^{jk\omega_b t}. \tag{34}$$

Introducing (34) in (14), the unperturbed voltage becomes

$$v(t) = 2Re\left\{V(t)e^{j\omega t}e^{j\phi(t)}\right\} = \sum_{k=-\infty}^{\infty} X_k e^{j(\omega t + k\omega_b t)} \tag{35}$$

where X_k is the harmonic component resulting from the time-varying amplitude and phase components $V(t)$ and $\phi(t)$. To address the phase-noise analysis, we will take into account that the system is autonomous in ω_b. Applying Dirichlet's theorem [51], it can be deduced that the injected oscillator system is invariant under any constant phase shift α in its autonomous components [33]. Thus, any steady-state solution of the form, the following equation will necessarily fulfill the system equations:

$$v(t,\alpha) = \sum_{k=-\infty}^{\infty} X_k e^{j(\omega t + k(\omega_b t + \alpha))} = 2\text{Re}\left\{V(t + \alpha/\omega_b)\exp\left(j\left(\omega t + \phi(t + \alpha/\omega_b)\right)\right)\right\}. \tag{36}$$

Then, in the presence of the noise sources, the perturbed solution can be expressed as follows:

$$v(t) = \left(V(t + \delta\varphi(t)/\omega_b) + \delta V(t)\right) \times \exp\left(j\left(\omega t + \phi(t + \delta\varphi(t)/\omega_b)\right)\right). \tag{37}$$

As observed in the first line of (36), the phase perturbation affecting each kth harmonic component is $k\delta\varphi(t)$, which leaves the component at the input frequency ($k = 0$) unperturbed.

To get analytical insight, the derivation will make use of the linearized admittance function Y, with derivatives $\partial Y_o/\partial V$ and $\partial Y_o/\partial\omega$ extracted from HB through finite differences. The noise perturbation will be modeled with the equivalent noise source $I_n(t) = I_{n,r}(t) + jI_{n,i}(t)$. The value of this equivalent source, connected in parallel at the analysis node, is obtained

through the fitting procedure described in [52]. We obtain a single equivalent noise current source from the simulation of the standalone free-running oscillator at the circuit level. This equivalent current source is connected in parallel to the analysis node. To obtain its spectral density, we perform a detailed simulation of the phase-noise spectrum of the standalone free-running oscillator, considering all the noise sources existing in the transistor model. They correspond to a gate current white noise source and a drain current noise source, accounting for white and flicker noise, as well as thermal noise generated by the resistors.

Introducing the equivalent current noise source in the semi-analytical formulation (1), we obtain

$$\begin{aligned}
&\frac{\partial Y^r\left[V_o(\eta),\omega_o(\eta)\right]}{\partial V}\left[V(t+\chi)+\delta V(t)-V_o(\eta)\right]\\
&\quad+\frac{\partial Y^r\left[V_o(\eta),\omega_o(\eta)\right]}{\partial \omega}\left[\omega+\frac{d\phi(t+\chi)}{dt}-\omega_o(\eta)\right]\\
&\quad=\frac{I_g}{V_o}\cos\left[\phi(t+\chi)\right]+\frac{I_{n,r}(t)}{V_o}\\
&\frac{\partial Y^i\left[V_o(\eta),\omega_o(\eta)\right]}{\partial V}\left[V(t+\chi)+\delta V(t)-V_o(\eta)\right]\\
&\quad+\frac{\partial Y^i\left[V_o(\eta),\omega_o(\eta)\right]}{\partial \omega}\left[\omega+\frac{d\phi(t+\chi)}{dt}-\omega_o(\eta)\right]\\
&\quad=-\frac{I_g}{V_o}\sin\left[\phi(t+\chi)\right]+\frac{I_{n,i}(t)}{V_o}
\end{aligned}\tag{38}$$

where $\delta\varphi(t)$ and $\delta V(t)$ are the phase and amplitude perturbations, $\chi(t)=\delta\varphi/\omega_b$ is the stochastic time perturbation, and we have neglected the time derivative $d[\delta V(t)]/dt$. Expanding in a first-order Taylor series the sinusoidal terms, we get

$$\delta\dot{\varphi}(t)=a\left[\phi(t)\right]\Delta\phi(t)+\bar{h}\left[\phi(t)\right]^t\begin{pmatrix}I_{n,r}(t)\\ I_{n,i}(t)\end{pmatrix}\tag{39}$$

where

$$\begin{aligned}
a\left[\phi(t)\right]&=-\omega_b\left(B(\eta)\cos\left[\phi(t)+\alpha_v(\eta)\right]+\ddot{\phi}(t)/\phi(t)\right)\\
\bar{h}\left[\phi(t)\right]&=-\frac{\omega_b}{\dot{\phi}(t)}\frac{\begin{pmatrix}\sin\left[\phi(t)\right] & \cos\left[\phi(t)\right]\\ -\cos\left[\phi(t)\right] & \sin\left[\phi(t)\right]\end{pmatrix}\begin{pmatrix}\frac{\partial Y_o^r(\eta)}{\partial V}\\ \frac{\partial Y_o^i(\eta)}{\partial V}\end{pmatrix}}{V_o(\eta)\left|\frac{\partial Y_o(\eta)}{\partial V}\right|\left|\frac{\partial Y_o(\eta)}{\partial \omega}\right|\sin\alpha_{v\omega}(\eta)}.
\end{aligned}\tag{40}$$

Expression (39) is a stochastic differential equation with time-periodic coefficients at the beat frequency. Thus, both the phase perturbation and the noise source can be expressed in a Fourier series as

$$\delta\varphi(t)=\sum_{k=-\mathrm{NH}}^{\mathrm{NH}}\Delta\Phi_k(t)e^{jk\omega_b t}\tag{41a}$$

$$I_n(t)=\sum_{k=-\mathrm{NH}}^{\mathrm{NH}}N_k(t)e^{jk\omega_b t}.\tag{41b}$$

The harmonic terms in the above expressions are slowly varying, with their spectra confined in the interval $(-\omega_b/2, \omega_b/2]$ as follows:

$$\begin{aligned}
\Delta\Phi_k(t)&=\lim_{T\to\infty}\int_{-\omega_b/2}^{\omega_b/2}\Delta\tilde{\phi}(\Omega+k\omega_b,T)e^{j\Omega t}d\Omega\\
N_k(t)&=\lim_{T\to\infty}\int_{-\omega_b/2}^{\omega_b/2}\tilde{I}_n(\Omega+k\omega_b,T)e^{j\Omega t}d\Omega
\end{aligned}\tag{42}$$

where we have used the following notation for the frequency-domain representation of any time-domain signal $x(t)$:

$$\tilde{x}(\Omega,T)=\int_{-T/2}^{T/2}x(t)e^{-j\Omega t}dt.\tag{43}$$

Now, introducing (41) in (39) and translating the time-varying harmonics $\Delta\Phi_k(t)$ and $N_k(t)$ to the frequency domain using (43), we obtain the following relationship:

$$\Delta\tilde{\Phi}(\Omega,T)=A(\Omega)\tilde{N}(\Omega,T)\tag{44}$$

where $\Delta\tilde{\Phi}(\Omega,T)$ and $\tilde{N}(\Omega,T)$ are, respectively, the vectors containing the components $\Delta\tilde{\Phi}(\Omega,T)$ and $\tilde{N}_k(\Omega,T)$ for $k=-\mathrm{NH},\ldots,\mathrm{NH}$. In turn, the matrix $A(\Omega)$ is given by

$$A(\Omega)=\left(\left[j\bar{k}\omega_b+\Omega\right]-T_a\right)^{-1}\begin{pmatrix}T_{h_1} & T_{h_2}\end{pmatrix}.\tag{45}$$

In the above expression, $[j\bar{k}\omega_b+\Omega]$ is a diagonal matrix with $k=-\mathrm{NH},\ldots,\mathrm{NH}$, and T_a, T_{h_1}, and T_{h_2} are the Toeplitz matrices [23] associated with $a[\phi(t)]$ and the two components of the vector $\bar{h}[\phi(t)]$. The phase noise about the component ω_b can be approached by the PSD of the phase perturbation process $\delta\varphi(t)$, which is calculated from 41(a) as follows:

$$\begin{aligned}
&S_{\delta\varphi}(\Omega)\\
&=\lim_{T\to\infty}\frac{1}{T}\left\langle|\delta\tilde{\varphi}(\Omega,T)|^2\right\rangle\\
&=\lim_{T\to\infty}\frac{1}{T}\sum_{k,l=-\mathrm{NH}}^{\mathrm{NH}}\left\langle\Delta\tilde{\Phi}_k(\Omega-k\omega_b,T)\Delta\tilde{\Phi}_l(\Omega-l\omega_b,T)^*\right\rangle.
\end{aligned}\tag{46}$$

Expansion (46) can be simplified taking into account that $I_{n,r}(t)$ and $I_{n,i}(t)$ are uncorrelated white noise processes fulfilling $\langle I_n(t_1)I_n(t_2)^*\rangle=\Gamma\delta(t_1-t_2)$, which implies

$$\lim_{T\to\infty}\left\langle\tilde{N}_k(\Omega_1,T)\,\tilde{N}_l(\Omega_2,T)^*\right\rangle=\Gamma\delta_k^l\delta(\Omega_1-\Omega_2)\tag{47}$$

where $k,l=-\mathrm{NH},\ldots,\mathrm{NH}$, δ_k^l is the Kronecker delta, and we have considered the bandwidth limitation of $N_k(t)$

$$\lim_{T\to\infty}\tilde{N}_k(\Omega,T)=\begin{cases}\lim_{T\to\infty}\tilde{I}_n(\Omega+k\omega_b,T), & |\Omega|<\omega_b/2\\ 0, & |\Omega|\geq\omega_b/2.\end{cases}\tag{48}$$

Because of (47), the terms $\Delta\tilde{\Phi}_k$ and $\Delta\tilde{\Phi}_m$, where $k\neq m$, are uncorrelated. Then, using (44) and applying (47), the PSD in (46) becomes

$$\begin{aligned}
S_{\delta\varphi}(\Omega)&=\lim_{T\to\infty}\frac{1}{T}\sum_{k=-\mathrm{NH}}^{\mathrm{NH}}\left\langle\left|\Delta\tilde{\Phi}_k(\Omega-k\omega_b,T)\right|^2\right\rangle\\
&=\sum_{k=-\mathrm{NH}}^{\mathrm{NH}}C_{k,k}(\Omega-k\omega_b)
\end{aligned}\tag{49}$$

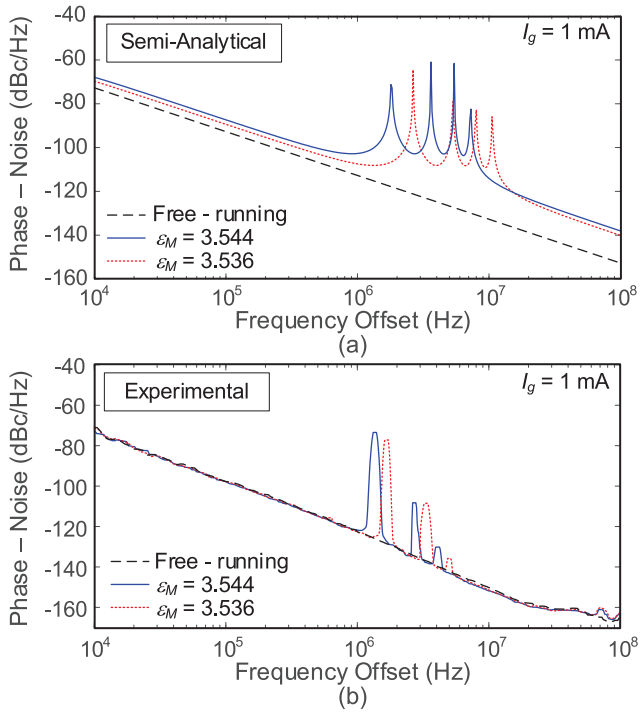

Fig. 14. Phase-noise spectrum of the injected oscillator for two values of the MUT dielectric constant: $\varepsilon_{M,1} = 3.544$ and $\varepsilon_{M,2} = 3.536$. (a) Analytical prediction through (49). (b) Measured phase-noise spectra for the same two dielectric samples (Rogers 4003C substrate) with sparse holes as in Fig. 9.

where each $C_{k,k}(\Omega - k\omega_b)$ is the kth component of the diagonal of the correlation matrix $C(\Omega - k\omega_b)$. This matrix is obtained from (44) as follows:

$$C(\Omega) = \lim_{T\to\infty} \frac{1}{T} \left\langle \Delta\tilde{\Phi}(\Omega, T)\Delta\tilde{\Phi}(\Omega, T)^{+} \right\rangle = \Gamma A(\Omega)A(\Omega)^{+}. \tag{50}$$

Note that (49) is composed by the translation of the spectra provided by the components $\langle|\Delta\tilde{\Phi}_k(\Omega, T)|^2\rangle$ to the frequencies $k\omega_b$, for $k = -N, \ldots, N$. The above method has been applied to calculate the phase-noise spectral density $S_{\delta\varphi}(\Omega)$ of the oscillator in Fig. 7 when operating under a low input amplitude. Note that this is required for the validity of the Taylor series expansion of the admittance function Y, on which the semianalytical formulation is based.

To validate the analysis, we have considered a solid substrate and two values of the MUT dielectric constant: $\varepsilon_{M,1} = 3.544$ and $\varepsilon_{M,2} = 3.536$, which provide the beat frequencies $f_{b,1} = 1.15$ MHz and $f_{b,2} = 1.77$ MHz, respectively. The analytical spectra obtained in the two cases are shown in Fig. 14(a). The reference frequency is the one corresponding to the frequency offset 0 Hz in the spectrum of Fig. 14. This reference frequency agrees with the difference between the input frequency and the beat frequency, $\omega - \omega_b$. Each spectrum contains resonances at the multiples $n\omega_b$. For a smaller ω_b, the resonances are closer, which gives rise to an increase in the phase-noise spectral density. Thus, the PSD is higher for $\varepsilon_{M,1} = 3.544$ (closer to the locking boundary) than for $\varepsilon_{M,2} = 3.536$. The phase noise is also compared with that of the standalone free-running oscillator, where the reference frequency is the free-running one. From the analytical study, we conclude that there may be a potential increase in phase noise compared to standalone free-running operation due to the resonances at $n\omega_b$, where n is an integer. In principle, this effect is expected to be more significant for smaller ω_b, as the resonances are closer together.

The results of the phase-noise analysis have been compared with the experimental measurements, obtained with the R&S FSWP8 phase-noise analyzer for the two ε_M values. They have been achieved by drilling holes in Rogers 4003C substrate, according to (33). The quantitative discrepancies with the semianalytical predictions arise from the accuracy limitations associated with neglecting the correlation between sidebands at different harmonic components of the beat frequency, as done in (46). However, there is good qualitative agreement, which enables an understanding of the phase-noise behavior. The phase noise increases for a lower ω_b due to the presence of the nearby resonances. Note that the phase-noise increase with respect to free-running operation is smaller in the experimental characterization. Outside the resonances, the PSD levels are very similar to those obtained in free-running conditions, which demonstrates the usability of this operation mode.

VI. Conclusion

This article presents a comprehensive study of a beat-frequency sensor based on an injected oscillator operating near its locking boundaries. Under these conditions, the beat frequency exhibits significantly higher sensitivity to the MUT compared to the free-running oscillation frequency. We have derived a general expression for the beat frequency, which is influenced by the MUT and determined through an admittance function obtainable from HB simulations. We have also introduced a method for establishing the locking boundary at a value suitable for the anticipated MUT variations. For the first time, to our knowledge, we have carried out a detailed investigation of the oscillator phase noise near the locking boundaries. This is based on a Fourier-series representation of the phase perturbation that allows the derivation of an equation relating its PSD with that of the oscillator noise sources in terms of Toeplitz matrices. This provides valuable insights into the impact of phase noise on the oscillator performance. The methods were illustrated through a cubic-nonlinearity oscillator and their application to a transistor-based oscillator with the MUT positioned over a capacitive transmission line. The sensitivity was evaluated in response to very small variations in the MUT's dielectric constant, achieved by drilling holes in a solid substrate and by adding drops of ethanol to a volume of deionized water. The sensitivity obtained is significantly higher than that achieved with a standalone free-running oscillator.

Acknowledgment

The authors would like to thank Eva Cuerno and Paul Garcia for their valuable help in the manufacture of the different prototypes.

References

[1] F. Martín, P. Vélez, J. Muñoz-Enano, and L. SU, *Planar Microwave Sensors*. Hoboken, NJ, USA: IEEE-Wiley, 2022.

[2] P. Casacuberta et al., "Sensitivity optimization in single-frequency planar microwave sensors for solid and liquid characterization and microfluidics," *IEEE Trans. Microw. Theory Techn.*, vol. 73, no. 3, pp. 1581–1609, Mar. 2025, doi: 10.1109/TMTT.2024.3452433.

[3] H. Yu, X. Ding, J. Chen, S. Sabbaghi, and Q. J. Gu, "Design and analysis of a sub-THz resonator-based high-resolution permittivity sensor," *IEEE Trans. Microw. Theory Techn.*, vol. 72, no. 5, pp. 2809–2823, May 2024.

[4] A. Ebrahimi and K. Ghorbani, "High-sensitivity detection of solid and liquid dielectrics using a branch line coupler sensor," *IEEE Trans. Microw. Theory Techn.*, vol. 71, no. 12, pp. 5233–5245, Dec. 2023.

[5] H. Hamzah, A. A. Abduljabar, and A. Porch, "High Q microwave microfluidic sensor using a central gap ring resonator," *IEEE Trans. Microw. Theory Techn.*, vol. 68, no. 5, pp. 1830–1838, May 2020.

[6] S. Mohammadi, K. K. Adhikari, M. C. Jain, and M. H. Zarifi, "High-resolution, sensitivity-enhanced active resonator sensor using substrate-embedded channel for characterizing low-concentration liquid mixtures," *IEEE Trans. Microw. Theory Techn.*, vol. 70, no. 1, pp. 576–586, Jan. 2022.

[7] Z. R. Omam, V. Nayyeri, S.-H. Javid-Hosseini, and O. M. Ramahi, "Simple and high-sensitivity dielectric constant measurement using a high-directivity microstrip coupled-line directional coupler," *IEEE Trans. Microw. Theory Techn.*, vol. 70, no. 8, pp. 3933–3942, Aug. 2022.

[8] D. L. Gershon, J. P. Calame, Y. Carmel, T. M. Antonsen, and R. M. Hutcheon, "Open-ended coaxial probe for high-temperature and broad-band dielectric measurements," *IEEE Trans. Microw. Theory Techn.*, vol. 47, no. 9, pp. 1640–1648, Sep. 1999.

[9] F. I. Jamal, S. Guha, M. H. Eissa, D. Kissinger, and J. Wessel, "A low-power 30 GHz complex dielectric chem-bio-sensor in a SiGe BiCMOS technology," in *IEEE MTT-S Int. Microw. Symp. Dig.*, Gothenburg, Sweden, May 2017, pp. 1–4.

[10] J. Wessel, K. Schmalz, J. C. Scheytt, B. Cahill, and G. Gastrock, "Microwave biosensor for characterization of compartments in Teflon capillaries," in *Proc. 42nd Eur. Microw. Conf.*, Amsterdan, The, Netherlands, Oct. 2012, pp. 534–537.

[11] C. H. Tseng, C. H. Pai, and H. C. Chang, "A new microwave oscillator-based microfluidic dielectric sensor," *IEEE Trans. Microw. Theory Techn.*, vol. 72, no. 1, pp. 628–637, Jan. 2024.

[12] J. Huang et al., "Oscillation-based active sensor on SIW reentrant cavity resonator for self-sustained ultralow concentration detection to saline solution," *IEEE Trans. Microw. Theory Techn.*, vol. 72, no. 9, pp. 5406–5419, Sep. 2024.

[13] A. A. Helmy et al., "A self-sustained CMOS microwave chemical sensor using a frequency synthesizer," *IEEE J. Solid-State Circuits*, vol. 47, no. 10, pp. 2467–2483, Oct. 2012.

[14] M. Pontón, S. Sancho, A. Herrera, and A. Suárez, "Oscillators based on step-impedance and slow wave transmission lines for sensing applications," *IEEE Trans. Microw. Theory Techn.*, vol. 71, no. 1, pp. 203–217, Jan. 2023.

[15] M. Babay et al., "Highly sensitive capacitive sensor based on injection locked oscillators with ppm sensing resolution," in *IEEE MTT-S Int. Microw. Symp. Dig.*, Los Angeles, CA, USA, Aug. 2020, pp. 456–459.

[16] M. Pontón, S. Hernández, and A. Suárez, "Phase-sensitivity analysis of injection-locked mutually coupled oscillators," in *Proc. 47th Eur. Microw. Conf. (EuMC)*, Nuremberg, Germany, Oct. 2017, pp. 771–774, doi: 10.23919/EuMC.2017.8230961.

[17] J. Juillard, P. Prache, and N. Barniol, "Analysis of mutually injection-locked oscillators for differential resonant sensing," *IEEE Trans. Circuits Syst. I, Reg. Papers*, vol. 63, no. 7, pp. 1055–1066, Jul. 2016, doi: 10.1109/TCSI.2016.2553298.

[18] M. Kanoun, B. P. S. Jadav, D. Cordeau, J.-M. Paillot, H. Mnif, and M. Loulou, "A 5.8 GHz fully integrated BiCMOS SiGe:C injection-locked-oscillator-based active phase shifter for energy beamforming," *Anal. Integr. Circuits Signal Process.*, vol. 106, no. 2, pp. 363–374, Jan. 2020, doi: 10.1007/s10470-020-01586-0.

[19] R. Mirzavand, M. M. Honari, and P. Mousavi, "High-resolution dielectric sensor based on injection-locked oscillators," *IEEE Sensors J.*, vol. 18, no. 1, pp. 141–148, Jan. 2018.

[20] J. Huang and Y. Xiang, "Injection-locked-oscillation-based active sensor on dual-mode folded SIW rectangular cavity for high-resolution detection to moisture and Fe particle in lubricant oil," *IEEE Trans. Microw. Theory Techn.*, vol. 71, no. 4, pp. 1600–1611, Apr. 2023.

[21] M. Pontón, A. Suarez, and S. Sancho, "Analysis of the nonlinear dynamics of an injection-locked dual-mode oscillator," *IEEE Trans. Microw. Theory Techn.*, vol. 72, no. 9, pp. 5120–5133, Sep. 2024.

[22] K. Huang and M. Hossein-Zadeh, "Detection and sensing using coupled oscillatory systems at the synchronization edge," *IEEE Sensors J.*, vol. 20, no. 21, pp. 12992–12998, Nov. 2020.

[23] Y. Kuramoto and H. Araki, "Self-entrainment of a population of coupled non-linear oscillators," in *Proc. Int. Symp. Math. Problems Theor. Phys.*, vol. 39, Aug. 2005, pp. 420–422.

[24] J. Guckenheimer and P. J. Holmes, *Nonlinear Oscillations, Dynamical Systems, and Bifurcations of Vector Fields*. New York, NY, USA: Springer, 1983.

[25] J. M. T. Thompson and H. B. Stewart, *Nonlinear Dynamics and Chaos*. New York, NY, USA: Wiley, 2002.

[26] B. Razavi, "A study of injection locking and pulling in oscillators," *IEEE J. Solid-State Circuits*, vol. 39, no. 9, pp. 1415–1424, Sep. 2004.

[27] R. Adler, "A study of locking phenomena in oscillators," *Proc. IRE*, vol. 34, no. 6, pp. 351–357, Jun. 1946.

[28] M. Armand, "On the output spectrum of unlocked driven oscillators," *Proc. IEEE*, vol. 57, no. 5, pp. 798–799, May 1969.

[29] M. Pontón, S. Sancho, A. Herrera, and A. Suárez, "Wireless injection locking of zero-IF self-oscillating mixers," *IEEE Trans. Microw. Theory Techn.*, vol. 70, no. 1, pp. 836–849, Jan. 2022.

[30] E. Ngoya and R. Larcheveque, "Envelop transient analysis: A new method for the transient and steady state analysis of microwave communication circuits and systems," in *IEEE MTT-S Int. Microw. Symp. Dig.*, vol. 3, Jun. 1996, pp. 1365–1368.

[31] N. B. Carvalho, J. C. Pedro, W. Jang, and M. B. Steer, "Nonlinear RF circuits and systems simulation when driven by several modulated signals," *IEEE Trans. Microw. Theory Techn.*, vol. 54, no. 2, pp. 572–579, Feb. 2006.

[32] F. K. Kärtner, "Analysis of white and f-α noise in oscillators," *Int. J. Circuit Theory Appl.*, vol. 18, pp. 485–519, Jan. 1990.

[33] V. Rizzoli and A. Neri, "Harmonic-balance analysis of multitone autonomous nonlinear microwave circuits," in *IEEE MTT-S Int. Microw. Symp. Dig.*, Boston, MA, USA, Jul. 1991, pp. 107–110.

[34] R. A. Horn and C. R. Johnson, *Matrix Analysis*. New York, NY, USA: Cambridge Univ. Press, 2013.

[35] R. Quere et al., "Large signal design of broadband monolithic microwave frequency dividers and phase-locked oscillators," *IEEE Trans. Microw. Theory Techn.*, vol. 41, no. 11, pp. 1928–1938, Nov. 1993.

[36] A. Suarez, J. Morales, and R. Quere, "Synchronization analysis of autonomous microwave circuits using new global-stability analysis tools," *IEEE Trans. Microw. Theory Techn.*, vol. 46, no. 5, pp. 494–504, May 1998.

[37] A. Suárez, *Analysis and Design of Autonomous Microwave Circuits*. New York, NY, USA: Wiley, 2009.

[38] K. Kurokawa, "Some basic characteristics of broadband negative resistance oscillator circuits," *Bell Syst. Tech. J.*, vol. 48, no. 6, pp. 1937–1955, Jul. 1969.

[39] M. Pontón and A. Suárez, "Wireless injection locking of oscillator circuits," *IEEE Trans. Microw. Theory Techn.*, vol. 64, no. 12, pp. 4646–4659, Dec. 2016.

[40] A. Ebrahimi, J. Scott, and K. Ghorbani, "Differential sensors using microstrip lines loaded with two split-ring resonators," *IEEE Sensors J.*, vol. 18, no. 14, pp. 5786–5793, Jul. 2018.

[41] C. Herrojo et al., "Highly sensitive defect detectors and comparators exploiting port imbalance in rat-race couplers loaded with step-impedance open-ended transmission lines," *IEEE Sensors J.*, vol. 21, no. 23, pp. 26731–26745, Dec. 2021.

[42] L. D. Landau and E. M. Lifshitz, *Electrodynamics of Continuous Media*. New York, NY, USA: Pergamon Press, 1984.

[43] A. Sihvola, *Electromagnetic Mixing Formulas and Applications*. London, U.K.: IET, 1999.

[44] M. Gil, P. Vélez, F. Aznar-Ballesta, J. Muñoz-Enano, and F. Martín, "Differential sensor based on electroinductive wave transmission lines for dielectric constant measurements and defect detection," *IEEE Trans. Antennas Propag.*, vol. 68, no. 3, pp. 1876–1886, Mar. 2020.

[45] A. Ebrahimi, G. Beziuk, J. Scott, and K. Ghorbani, "Microwave differential frequency splitting sensor using magnetic-LC resonators," *Sensors*, vol. 20, no. 4, p. 1066, Feb. 2020.

[46] G. Govind, N. K. Tiwari, K. K. Agrawal, and M. J. Akhtar, "Microwave imaging of subsurface defects in dielectric structures using complementary split ring resonator," in *Proc. 3rd Int. Conf. Microw. Photon. (ICMAP)*, Dhanbad, India, Feb. 2018, pp. 1–2.

[47] A. K. Jha, A. Lamecki, R. Gómez-García, and M. Mrozowski, "Near field coupled wireless microwave sensor," in *Proc. 23rd Int. Microw. Radar Conf. (MIKON)*, Warsaw, Poland, Oct. 2020, pp. 260–262.

[48] P. Vélez, X. Canalias, J. Muñoz-Enano, P. Casacuberta, L. Su, and F. Martín, "Effects of losses on the sensitivity of reflective-mode phase-variation liquid sensors," *IEEE Trans. Microw. Theory Techn.*, vol. 72, no. 2, pp. 903–918, Feb. 2024.
[49] J. MuñozEnano, P. Vélez, P. Casacuberta, L. Su, and F. Martín, "Reflective-mode phase-variation permittivity sensor based on a step-impedance microstrip line terminated with a slot resonator for solid and liquid characterization," *IEEE Trans. Microw. Theory Techn.*, vol. 72, no. 4, pp. 2519–2533, Oct. 2024.
[50] J.-Z. Bao, M. L. Swicord, and C. C. Davis, "Microwave dielectric characterization of binary mixtures of water, methanol, and ethanol," *J. Chem. Phys.*, vol. 104, no. 12, pp. 4441–4450, Mar. 1996.
[51] J. M. Lee, *Introduction to Smooth Manifolds*, 2nd ed., New York, NY, USA: Springer, 2013.
[52] F. Ramirez, M. Ponton, S. Sancho, and A. Suarez, "Phase-noise analysis of injection-locked oscillators and analog frequency dividers," *IEEE Trans. Microw. Theory Techn.*, vol. 56, no. 2, pp. 393–407, Feb. 2008.

Mabel Pontón (Member, IEEE) was born in Santander, Spain. She received the bachelor's degree in telecommunication engineering, the master's degree in information technologies and wireless communications systems, and the Ph.D. degree from the University of Cantabria, Santander, in 2004, 2008, and 2010, respectively.

In 2006, she joined the Communications Engineering Department, University of Cantabria. From 2011 to 2013, she was with the Group of Electronic Design and Applications, Georgia Institute of Technology, Atlanta, GA, USA, as a Post-Doctoral Research Fellow. Her current research interests include the nonlinear analysis and simulation of radio frequency and microwave circuits, with an emphasis on phase-noise, stability, and bifurcation analysis of complex oscillator topologies.

Sergio Sancho (Senior Member, IEEE) received the Licentiate degree in electronic physics from Basque Country University, Leioa, Spain, in 1997, and the Ph.D. degree in electronic engineering from the University of Cantabria, Santander, Spain, in February 2002.

In 1998, he joined the Communications Engineering Department, University of Cantabria, Santander, where he is currently an Associate Professor with the Communications Engineering Department. His research interests include the nonlinear analysis of microwave autonomous circuits and frequency synthesizers, including stochastic and phase-noise analysis.

Almudena Suárez (Fellow, IEEE) was born in Santander, Spain. She received the Licentiate degree in electronic physics and the Ph.D. degree from the University of Cantabria, Santander, in 1987 and 1992, respectively, and the Ph.D. degree in electronics from the University of Limoges, Limoges, France, in 1993.

She is currently a Full Professor with the University of Cantabria and the Head of the Research Group Microwave Engineering and Radiocommunication Systems. She has authored the book *Analysis and Design of Autonomous Microwave Circuits* (IEEE-Wiley, 2009) and co-authored the book *Stability Analysis of Nonlinear Microwave Circuits* (Artech House, 2003).

Prof. Suárez is a member of the Technical Committee of the IEEE International Microwave Symposium (IEEE MTT-S) and the European Microwave Week. She is a member of the Board of Directors of European Microwave Association. She was the Coordinator of the Communications and Electronic Technology Area for Spanish National Evaluation and Foresight Agency (ANEP) from 2009 to 2013. She was the Chair of the 2014 and 2015 editions of the IEEE Topical Conference on RF/Microwave Power Amplifiers (PAWR), in Newport Beach and San Diego. She was the General TPC Chair of European Microwave Week 2018. She was the Editor-in-Chief of the *International Journal of Microwave and Wireless Technologies* from Cambridge University Press journals from 2013 to 2018. She is currently an Associate Editor of *IEEE Microwave Magazine* and IEEE TRANSACTIONS ON MICROWAVE THEORY AND TECHNIQUES. She was the Chair of the IEEE Subcommittee for the Best Paper Award in *IEEE Microwave Magazine* from 2017 to 2020. She was an IEEE Distinguished Microwave Lecturer from 2006 to 2008.